University of Helsinki Report Series in Physics

HU-P-D253

Inelastic, non-diffractive and diffractive proton-proton cross-section measurements at the LHC

Jan Welti

Department of Physics
and
Helsinki Institute of Physics
Faculty of Science
University of Helsinki
Helsinki, Finland

ACADEMIC DISSERTATION

To be presented, with the permission of the Faculty of Science of the University of Helsinki, for public criticism in the lecture hall A111 of Exactum (Gustaf Hällströmin katu 2b, Helsinki) on Friday, 3rd of November 2017 at 12 o'clock noon.

Helsinki 2017

Supervisor:
Professor Kenneth Österberg
University of Helsinki

Pre-examiners:
Professor Michele Arneodo
Università Del Piemonte Orientale, Italy

Professor David Milstead
Stockholms Universitet, Sweden

Opponent:
Professor Paul Newman
University of Birmingham, UK

Custos:
Professor Kenneth Österberg
University of Helsinki

ISBN 978-951-51-2775-4 (printed version)
ISBN 978-951-51-2776-1 (pdf)
ISSN 0356-0961
http://ethesis.helsinki.fi
Helsinki 2017
Unigrafia

Abstract

The energy dependence of the rates and cross-sections of proton-proton interactions is of high importance both for collider physics and astroparticle physics. These quantities cannot be calculated from perturbative quantum chromodynamics, which has led to the development of several different models and parametrisations, and further measurements are needed to improve them and to test their validity. The inelastic rate for proton-proton interactions was measured at 2.76, 7 and 8 TeV center of mass energies using the T1 and T2 detectors of the TOTEM experiment at the LHC. Total and inelastic cross-sections were obtained using the Optical Theorem and measuring the inelastic and elastic rates simultaneously. The inelastic cross-sections $\sigma_{\text{inel}} = 62.8 \pm 2.9\,\text{mb}$ at 2.76 TeV, $\sigma_{\text{inel}} = 72.9 \pm 1.5\,\text{mb}$ at 7 TeV and $\sigma_{\text{inel}} = 74.7 \pm 1.7\,\text{mb}$ at 8 TeV, show an increase of the cross-sections as a function of energy as expected.

The inelastic cross-section at 7 TeV was also measured using an alternative method based on the CMS luminosity to determine the cross-section from the inelastic rate, with no measurement of the elastic part needed. The result, $\sigma_{\text{inel}} = 73.7 \pm 3.4\,\text{mb}$ is compatible with the luminosity independent measurement. The cross-section obtained requiring particles in the instrumented region ($|\eta| \leq 6.5$) was $\sigma_{\text{inel},|\eta|\leq 6.5} = 70.5 \pm 2.9\,\text{mb}$. Using this and a measurement of the full inelastic cross-section based on elastic scattering, which contains no assumptions about low mass diffraction, an upper limit for low mass diffraction of $\sigma_{\text{inel},|\eta|>6.5} \leq 6.31\,\text{mb}$ was obtained at 95 % confidence level.

Likewise, the cross-sections of the individual inelastic processes, most importantly non-, single and double diffractive, cannot be calculated from first principles, but are of high importance for further improvements of the models and the modelling of cosmic air showers. They are difficult to measure since the differences in the experimental signatures between different processes can be small, even identical, in some parts of the phase space. A good detector coverage is therefore essential and the cross-sections are most efficiently determined from the data with the use of a multivariate analysis method in order to exploit even small differences between the processes.

The majority of diffractive events have a clear rapidity gap and hence an experimental definition, where diffractive events were defined as having a rapidity gap of at least three units, was used in order to avoid a model-dependent definition of diffraction. If the event had a proton at minimum or maximum pseudorapidity followed by a rapidity gap of at least three units, it was considered single diffractive, other events with such a gap double diffractive and the remaining events non-diffractive. The cross-sections obtained using a classifier based on boosted decision trees, on data recorded with the combined CMS and TOTEM detectors at $\sqrt{s} = 8\,\text{TeV}$ collision energy, were $\sigma_{\text{ND}} = 50.0 \pm 2.2\,\text{mb}$ for non-diffractive, $\sigma_{\text{SD}} = 16.0 \pm 3.5\,\text{mb}$ for single diffractive and $\sigma_{\text{DD}} = 8.7 \pm 0.9\,\text{mb}$ for double diffractive. These results are in agreement with other measurements using the same definitions and indicate larger diffractive cross-sections than predicted by most models.

Acknowledgements

The work was carried out at the University of Helsinki, Department of Physics, Division of Particle Physics and Astrophysics as well as the Helsinki Institute of Physics and the European Organization for Nuclear Research (CERN). The tools, facilities and various forms of support provided by these institutions have made this work possible.

I want to thank my supervisor Prof. Kenneth Österberg for his guidance in making this thesis. Our discussions in the process of making this thesis has increased my understanding in physics and helped me to learn new statistical and computational tools.

I thank Prof. David Milstead and Prof. Michele Arneodo for reviewing this thesis. Their time and insight allowed to reach this point.

The financial support for the work presented this thesis provided by the Finnish Academy of Science and Letters and the Waldemar von Frenckell Foundation is gratefully acknowledged.

I wish to thank all my co-authors and colleagues in Helsinki and in Geneva, including members from both TOTEM and CMS experiments.

Finally, I want to thank my family and friends for indirect support.

Publications

The research publications included in this thesis are:

I Antchev G. *et al.*: "Measurement of proton-proton inelastic scattering cross-section at $\sqrt{s} = 7$ TeV"
Europhys. Lett., **101** (2013) 21003
DOI: https://doi.org/10.1209/0295-5075/101/21003

II Antchev G. *et al.*: "Luminosity-independent measurements of total, elastic and inelastic cross-sections at $\sqrt{s} = 7$ TeV"
Europhys. Lett., **101** (2013) 21004
DOI: https://doi.org/10.1209/0295-5075/101/21004

III Antchev G. *et al.*: "Luminosity-independent measurement of the proton-proton total cross-section at $\sqrt{s} = 8$ TeV"
Phys. Rev. Lett., **111** (2013) 01200
DOI: https://doi.org/10.1103/PhysRevLett.111.012001

IV J. Welti and K. Österberg: "Inelastic event classification with 8 TeV p-p collisions at the LHC", CMS-AN-2016/340

V Antchev G. *et al.*: "Luminosity-independent measurements of total, elastic and inelastic cross-sections at $\sqrt{s} = 2.76$ TeV", *Preliminary public result.* (2017)

Author's contribution to the joint publications

The author did most of the work for the inelastic rate and cross-section measurements for **I** and **II** as well as a significant part of the article writing, especially for **I**. The author also did an independent effective luminosity integration for **I**, which was later cross-checked with the authors of the publication of the elastic cross-section measurement.

For **III** the author did the inelastic rate and cross-section measurements and wrote the parts concerning those measurements.

For **IV** the author did the work and the writing with some help from K. Österberg and useful input from R. Ciesielski and M. Ruspa. This analysis has been pre-approved for PhD thesis presentation by the FSQ group of the CMS Collaboration on 5.10.2016 and by the TOTEM Collaboration on 18.10.2016.

For **V** the author did the preliminary inelastic cross-section measurement and preliminary results are presented in this thesis. Results of this analysis have been approved for public presentation 7.3.2017 by the TOTEM Collaboration.

Contents

Introduction

The energy dependence of the rates and cross-sections of proton-proton (pp) and proton-antiproton ($p\bar{p}$) interactions is of high importance both for collider physics and particle astrophysics. Therefore, measurements of cross-sections for pp (and $p\bar{p}$) collisions have been done since the earliest days of particle physics. These cross-sections cannot be calculated from perturbative quantum chromodynamics (QCD), which has led to the development of several different models and parametrisations.

Many approaches have been used to describe previous measurements of the cross-sections, such as the ones done at the ISR in the 1970's[1, 2, 3], S$\bar{p}$pS in the 1980's[4] and Tevatron in the 1990's[5, 6], and the asymptotic behaviour of the cross-section has been studied ever since Mandelstam discovered his representation[7] for the amplitudes of two-body reactions[8]. The high energy evolution of the cross-sections is bounded by the Froissart-bound due to considerations of unitarity and analycity. This bound is not dependent on the dynamics of the interaction. The result obtained by Froissart states that the total cross-section cannot rise faster than $(\frac{\pi}{m_\pi^2})\ln^2(s)$, where s is the center of mass energy squared and m_π is the pion mass. A similar limit also exists separately for the inelastic cross-section, $(\frac{\pi}{4m_\pi^2})\ln^2(s)$, which is four times smaller than the one for the total cross-section[9]. The constant $(\frac{\pi}{m_\pi^2})$ is an upper limit and in reality the rise of the cross-section can be slower. Experimental data show an increase in the total pp cross-section as a function of s, but it is not certain whether the asymptotic behaviour has already been reached.

Some of the most common models use a simple power law to describe the rise of the total cross-section. Some other models use QCD for some aspects of the calculations. Measurements at higher energies, including those at the LHC, some of which are presented in this thesis, are needed to improve the understanding of the more precise nature of the energy dependences of the pp and $p\bar{p}$ cross-sections.

The cross-sections of the individual inelastic processes, most importantly single, double and non-diffractive, cannot be calculated from perturbative QCD. In order to measure them, a multivariate analysis method can be applied combining data from multiple detectors, to classify events even based on small differences. Based on the classification the fractions of individual processes can be determined and using the total inelastic cross-section as normalization the cross-sections of the individual processes are obtained.

The amount of diffraction, especially at low mass, is of high importance when

modelling cosmic rays. Experimental measurements of high energy cosmic rays (energies above 10^{14} eV) are based on an indirect method, where properties of primary particles are reconstructed from properties of extensive air showers (EAS) induced by the cosmic rays in the atmosphere. The quality of the data depends heavily on the understanding of EAS physics. [10] The understanding of inelastic processes and their cross-sections is of high importance for improving the understanding of the structure of the proton, such as gluon density and correlations.

In the first chapter of this thesis, the theoretical background is given for the results presented and methods used in this thesis. An overview of the accelerator and experiment used for the measurements is provided in the second chapter. The third chapter gives an overview of the Monte Carlo event generators used to obtain the model expectations. Chapters four and five present the inelastic cross-section measurements and the classification of inelastic events, respectively. Conclusions from the measurements and outlook for future measurements are discussed at the end of the thesis.

Chapter 1

Theory

1.1 Mandelstam variables

Mandelstam variables, introduced in 1958 by Stanley Mandelstam, are Lorentz-invariant variables, which means that the values of the variables are independent of the chosen reference frame. They give information about energies, momenta and scattering angles of particles in a scattering process. Due to their Lorentz-invariance they are often more convenient to use than the angles and momenta of the interactions. [11]

The Mandelstam variables t and s are used in this thesis. They represent the squares of the four-momentum transfer and the center of mass energy, respectively.

With the Minkowski metric defined as

$$\eta^{\mu\nu} = \begin{pmatrix} 1 & 0 & 0 & 0 \\ 0 & -1 & 0 & 0 \\ 0 & 0 & -1 & 0 \\ 0 & 0 & 0 & -1 \end{pmatrix}, \tag{1.1}$$

the variables are given by

$$t = (p_1 - p_3)^2 = (p_2 - p_4)^2 \tag{1.2}$$

and

$$s = (p_1 + p_2)^2 = (p_3 + p_4)^2, \tag{1.3}$$

where p_1 and p_2 are the four-momenta of the initial state particles and p_3 and p_4 those of the final state particles. These relations apply for all 2-to-2 particle processes and in the case of elastic scattering the initial and final state particles are the same.

1.2 The Optical Theorem

TOTEM uses methods derived from the Optical Theorem to determine the total cross-section σ_{tot} and the integrated luminosity $\mathcal{L}_{\text{int}}$, which is also measured by CMS. The Optical Theorem is derived from an important property of the scattering matrix (S-matrix), that is the requirement that the sum of the probabilities of all final states must be equal to one. This is a consequence of the conservation of probability.

This requirement can be expressed for final states f and initial state i as follows [12].

$$\sum_f |\langle f|S|i\rangle|^2 = 1 \tag{1.4}$$

Using orthonormality this can be split in the following equations.

$$\sum_f \langle f|S|i\rangle \left(\langle f|S|i'\rangle\right)^* = \delta_{i,i'} \tag{1.5}$$

$$\sum_i \langle f|S|i\rangle \left(\langle f'|S|i\rangle\right)^* = \delta_{f,f'} \tag{1.6}$$

The previous formulae can also be written using matrix notation.

$$S^*S = SS^* = 1 \tag{1.7}$$

This implies that the S-matrix is a unitary matrix. The corresponding formula for the transition matrix T is:

$$\langle f|S|i\rangle = \delta_{f,i} + i(2\pi)^4\delta(Q^{(i)} - Q^{(f)})N_iN_f \langle f|T|i\rangle \,. \tag{1.8}$$

Here $Q^{(i)}$ and $Q^{(f)}$ are the four-momentum vectors of the initial and final states, respectively, and N_i and N_f normalization factors. Now equation 1.7 gives:

$$\begin{aligned}\delta_{f,i} = \delta_{f,i} + i(2\pi)^4\delta(Q^{(i)} - Q^{(f)})N_iN_f(\langle f|T|i\rangle - \langle i|T^*|f\rangle) + \\ + (2\pi)^8 N_iN_f \sum_a N_a^2\delta(Q^{(i)} - Q^{(a)})\delta(Q^{(a)} - Q^{(f)}) \langle f|T|a\rangle \langle a|T^*|i\rangle\end{aligned} \tag{1.9}$$

$$\Im\,|\langle f|T|i\rangle| = \frac{1}{2}(2\pi)^4 \sum N_a^2\delta(Q^{(i)} - Q^{(f)}) \langle f|T|a\rangle \langle a|T^*|i\rangle \,, \tag{1.10}$$

where $\Im$ stands for the imaginary part. $\Re$ will be used for the real part.

An important case is when the final and initial states are the same, $i\rangle = f\rangle$. Using the normalization $N_a^2 = \prod_i^n \frac{1}{2VE_i}$, where V is an arbitrary normalization volume and E_i the energy of the i:th particle in state a_n, replacing the sum over states a with n three-dimensional integrals over the momenta of the particles (with masses m_i and momenta q_i) and taking the limit when V goes to infinity leads to the following expression:

$$\Im\,|\langle i|T|i\rangle| = \frac{1}{2}\frac{1}{(2\pi)^{3n-4}} \int \cdots \int dq_1 \cdots dq_n \prod_{i=1}^n \delta(q_i^2 + m_i^2)\theta(q_i)\times$$

$$\times \delta(Q^{(i)} - \sum_i^n q_i)| \langle a_n|T|i\rangle |^2, \tag{1.11}$$

where

$$\theta(q_i) = \begin{cases} 0 & |q_i| < 0 \\ 1 & |q_i| \geq 0 \end{cases}.$$

The formula for the cross-section of the $a + b \to c + d$ process, where particles a and b have masses m_a and m_b and momenta p_a and p_b, is [12]

$$\sigma_{tot} = \frac{1}{2\sqrt{\lambda(s, m_a^2, m_b^2)}} \frac{1}{(2\pi)^{3n-4}} \int \cdots \int dq_1 \cdots dq_n \prod_{i=1}^{n} \delta(q_i^2 + m_i^2)\theta(q_i) \times$$

$$\times \delta(p_a + p_b - \sum_i^n q_i) \sum_{\text{spin}} | \langle f|T|i\rangle |^2, \tag{1.12}$$

where $\lambda(x, y, z) = x^2 + y^2 + z^2 - 2xy - 2xz - 2yz$. Combining equation 1.12 with equation 1.11, now assuming a 2-to-2 particle process, leads to the result

$$\Im\left[\langle i|T|i\rangle\right] = \Im(f_{\text{el}}(0)) = \sqrt{\lambda(s, m_i^2, M_i^2)}\sigma_{\text{tot}}, \tag{1.13}$$

where m_i and M_i are the masses of the two colliding particles. This formula is known as the Optical Theorem.

The following relation applies for the elastic cross-section:

$$\left.\frac{d\sigma_{\text{el}}}{dt}\right|_{t=0} = \frac{|T|^2}{16\pi\lambda(s, m_i^2, M_i^2)}. \tag{1.14}$$

Combining the two previous formulae (1.13 and 1.14) gives a relation between total cross-section and the nuclear part of the elastic cross-section $d\sigma_{\text{el}}/dt$ extrapolated to zero momentum transfer; this point is known as the optical point.

$$|T|^2 = 16\pi\lambda(s, m_i^2, M_i^2) \left.\frac{d\sigma_{\text{el}}}{dt}\right|_{t=0}$$

$$|T|^2 = (\Im[T])^2 + (\mathcal{R}[T])^2$$

$$\sigma_{\text{tot}}^2 = \frac{(\Im[T])^2}{\lambda(s, m_i^2, M_i^2)} = \frac{|T|^2 - (\mathcal{R}[T])^2}{\lambda(s, m_i^2, M_i^2)} = \frac{|T|^2}{\lambda(s, m_i^2, M_i^2)} - \frac{(\mathcal{R}[T])^2}{(\Im[T])^2}\sigma_{\text{tot}}^2$$

Defining $\rho = \mathcal{R}[T]/\Im[T]$, this can be written in the form shown below.

$$\sigma_{\text{tot}}^2 = 16\pi \left.\frac{d\sigma_{\text{el}}}{dt}\right|_{t=0} - \rho^2\sigma_{\text{tot}}^2$$

$$\sigma_{\text{tot}}^2 = \frac{16\pi}{1+\rho^2} \left.\frac{d\sigma_{\text{el}}}{dt}\right|_{t=0} \tag{1.15}$$

The parameter value $\rho \sim 0.14$ was taken from theoretical predictions[13] for the initial cross-section measurements and was later directly measured by TOTEM to be $\rho = 0.12 \pm 0.03$ at 8 TeV collision energy[14]. Since $\rho << 1$, it has a small impact due to the term $1 + \rho^2$ being the only term with dependence on ρ. This allows to measure the total and elastic cross-sections and deduce the inelastic as their difference.

Using the relation $\mathcal{L} d\sigma_{\text{el}}/dt = dN_{\text{el}}/dt$ between cross section σ, integrated luminosity $\mathcal{L}$ and number of elastic events N_{el} , the following useful formula is derived.

$$\mathcal{L}\sigma_{\text{tot}}^2 = \frac{16\pi}{1+\rho^2} \cdot \left.\frac{dN_{\text{el}}}{dt}\right|_{t=0} \tag{1.16}$$

An additional relation for the cross-section and the luminosity is given by the elastic and inelastic rates N_{el} and N_{inel} as follows.[15]

$$\mathcal{L}\sigma_{\text{tot}} = N_{\text{el}} + N_{\text{inel}} \tag{1.17}$$

This form of the equation depends on the direct measurements of the integrated elastic and inelastic rates as well as the integrated luminosity, but does not require information about the ρ-parameter and is independent of the Optical Theorem.

Cross-section and luminosity can be obtained by solving the system of equations given by 1.16 and 1.17. Solving the set of equations for σ_{tot} and $\mathcal{L}$ independently gives the following.

$$\sigma_{\text{tot}} = \frac{16\pi}{1+\rho^2} \cdot \frac{dN_{\text{el}}/dt|_{t=0}}{N_{\text{el}} + N_{\text{inel}}} \tag{1.18}$$

$$\mathcal{L} = \frac{1+\rho^2}{16\pi} \cdot \frac{(N_{\text{el}} + N_{\text{inel}})^2}{dN_{\text{el}}/dt|_{t=0}} \tag{1.19}$$

The cross-section and integrated luminosity can thus be calculated by measuring the inelastic rate N_{inel} (measured using the T1 and T2 tracking telescopes, see Sec. 2.2), the total nuclear elastic rate N_{el} (measured with Roman Pot detectors, see Sec. 2.2) and the optical point $dN_{\text{el}}/dt|_{t=0}$ (extrapolated from differential cross-section $d\sigma/dt$ measured with Roman Pots). In this case the inelastic part needs to be measured, but this allows to determine both the cross-sections and the luminosity without using the separate luminosity measurement from CMS.

These different methods allow to measure the total, elastic and inelastic cross-sections and the integrated luminosity. Having different methods to determine the cross-sections is a valuable cross-check of the results.

1.3 Interaction processes

In this section, the most important processes that make up the total pp cross-section are introduced. The most prominent interaction processes in pp collisions are elastic scattering, non-diffractive inelastic as well as single, double and central

diffractive. Higher order processes, which are less common, are not presented in detail.

In elastic scattering, the initial state protons and the absolute values of their momenta remain intact, but their directions are changed through a colourless exchange. A colourless exchange does not change the quantum numbers of the interacting systems. Elastic events have two back-to-back protons in the final state, typically at very small scattering angles. All other processes are considered inelastic; the protons can dissociate and new particles are produced in the final state.[16]

Diffractive processes are mediated by a colourless exchange, just like elastic scattering, which is in fact also considered a diffractive process. The object that mediates the interaction is called a pomeron. In terms of QCD, the pomeron is interpreted as a colour neutral gluon system, such as a gluon pair or ladder [17]. In non-diffractive inelastic scattering the exchange can carry colour. The phase-space of the final state of non-diffractive interactions is typically filled with particles; rapidity gaps, which are regions of rapidity space with no final state particles, can occur, but they are exponentially suppressed. On the other hand, in diffractive processes rapidity gaps are not exponentially suppressed and are observed in the majority of events.

Single, double and central diffractive processes have different final states. In single diffractive, one of the initial state protons remains intact and the other one dissociates and hadronizes, resulting in a final state with a forward proton on one side and a system of particles on the other side, with the two sides separated by a rapidity gap. In double diffractive, both initial state protons dissociate and hadronize, resulting in systems of particles on both sides of the rapidity gap. In central diffractive (also called Double Pomeron Exchange), the protons remain intact but a system of particles is produced in the central region, with rapidity gaps between both protons and the central system. The invariant mass of the hadronized system X or Y is called the diffractive mass, often denoted M_{X} or M_{Y}.

The rapidity gap of a diffractive event is related to the mass of the diffractive system. The average gap width for high mass single diffractive events is $\Delta\eta \approx \ln(s/M_{\mathrm{X}}^2) = -\ln\xi$, where M_{X} is the mass of the diffractive system and ξ the fractional momentum loss of the forward proton. In double diffractive events the gap is on average $\Delta\eta \approx \Delta y \approx \ln(ss_0/(M_{\mathrm{X}}^2 M_{\mathrm{Y}}^2))$, with $s_0 = 1\,\mathrm{GeV}$, y the gap in true rapidity and M_{X} and M_{Y} the diffractive masses of the two diffractive systems [18]. It can be seen from the equations that small diffractive masses are typically accompanied by a large rapidity gap and, in the case of single diffraction a small fractional momentum loss of the forward proton. Various properties of diffraction, including differential cross-sections and energy flow, have been measured at HERA in photoproduction $\gamma p \to XY$ [19] and deep inelastic electron-proton scattering $ep \to eXY$ [20, 21, 22].

Some examples of the processes mentioned here and an example of a higher order diffractive process (Multi-Pomeron exchange) are depicted in Fig. 1.1.

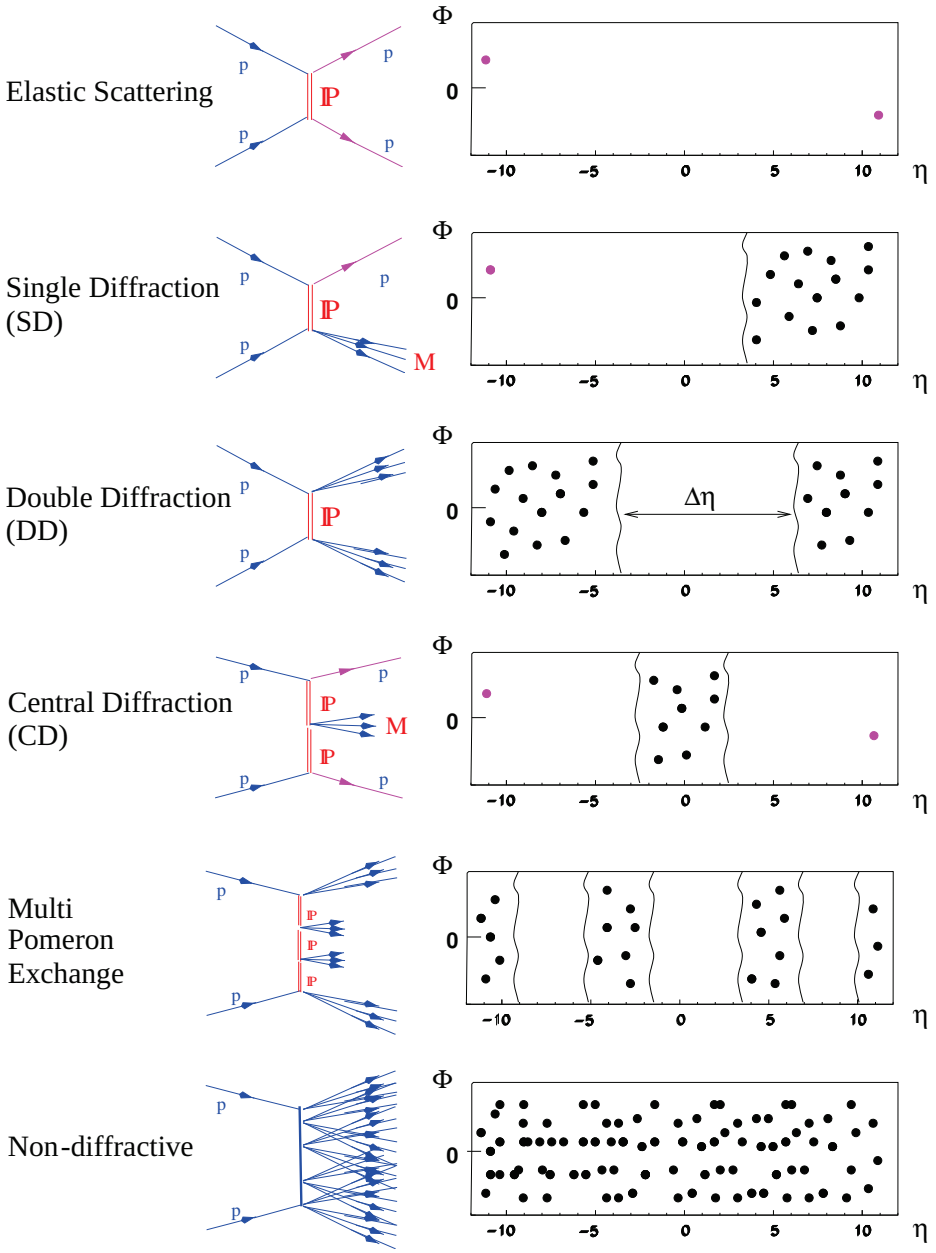

Figure 1.1: Schematic figures depicting typical events of different classes and the distribution of particles in the pseudorapidity η and azimuthal angle Φ -plane.

1.4 Classification

Several multivariate methods, that allow classification of unknown events through the use of training samples of known classes, have been invented. A very classical example is the Fisher Linear Discriminant [23], which gives the optimal linear separation between two classes. In cases where non-linear separation gives better performance or multiple classes exist, there are more novel methods, such as the boosted decision trees (BDTs) [24] and artificial neural networks (ANNs) [25].

Most classifiers can be used for binary (two-class) problems. In the case of more than two classes either one of the methods that natively support multiple class problems is needed or the problem is split into several binary problems by using a binarization technique. Several such techniques exist and in this work ordered binarization was used. In this technique the problem is reduced into several problems of the type "signal class versus all remaining backgrounds", for which the classification is executed in a predefined order. After each step the signal class is eliminated from the remaining classes and therefore the problem is gradually reduced from an N class problem into a binary problem and the total number of classifiers needed is $N-1$. In this work a binary classifier together with ordered binarization was used, since the other classifiers and binarization techniques used gave inferior separation. [26]

The output x of a classifier is often not directly the probability of the event to belong to a certain class, but a variable that is distributed between some minimum value x_{min} and some maximum value x_{max}, where low outputs are assigned to events that are background-like and high outputs to signal-like and ambiguous events get values between the two extremes. This output was in this work converted to a signal probability P_{sig} by using the following equation, based on Bayes' theorem for continuous variables [27]:

$$P_{\mathrm{sig}}(x) = \frac{p_{\mathrm{sig}} \int_{x_{\mathrm{min}}}^{x} f_{\mathrm{sig}}(x)dx}{p_{\mathrm{sig}} \int_{x_{\mathrm{min}}}^{x} f_{\mathrm{sig}}(x)dx + (1-p_{\mathrm{sig}}) \int_{x}^{x_{\mathrm{max}}} f_{\mathrm{bkg}}(x)dx}, \tag{1.20}$$

where p_{sig} is the prior probability of signal class events in the sample and $f_{\mathrm{sig}}(x)$ and $f_{\mathrm{bkg}}(x)$ the probability distribution functions (PDFs) for signal and background. Estimates of the probability distribution functions were obtained by using histograms of classifier outputs for the signal and background events as taken from the simulated training samples. The PDFs in the formula are integrated from least probable value to observed value for both classes; this represents the probability that an event is observed at x if it indeed is either signal or background. For signal and background the integration limits are different, since background is more probable at low x and signal at high.

1.4.1 Boosted decision trees

A decision tree is a binary classifier, with a tree-like structure. Left/right cuts are done repeatedly on a single variable at a time, until one of the stopping criteria is

fulfilled. The phase space is thus divided into several regions, which are designated to either signal or background class, depending on which class is represented by the majority of training events in the final node. An example of a decision tree is shown in Fig. 1.2. [28]

Boosting is a technique, which extends the concept from one tree to several trees, which together form a forest. The same training events are used for all trees and the result from all trees is eventually combined into a single classifier by taking a weighted average over the individual trees. Boosting improves the performance and stabilizes response with respect to fluctuations in the training sample compared to using a single tree.

An advantage of a traditional decision tree is that it allows a straight-forward interpretation because it can be visualized as a two-dimensional tree structure. Traditional decision trees can, however, suffer from instability with respect to statistical fluctuations in the training sample. A fluctuation in the training sample can result in a cut in an non-optimal variable, which can result in the whole tree structure below the node being altered.

This problem is reduced when a forest of trees is used. Boosting of the events modifies their weights in the training sample and improves statistical stability of the decision tree and improves classification performance compared to an individual tree. Typically boosting is used together with small trees, with tree depth of three to six, which are individually weak classifiers. Limiting the tree depth almost completely eliminates the tendency of overtraining.

The boosting technique used in this classification analysis is stochastic gradient boosting. The final classification function $F(x)$, which is an estimator for the true value y, is assumed to be a weighted sum of parametrised base functions $f(x; a_m)$, which are the individual decision trees. Each base function in this additive expansion corresponds to a unique decision tree.

$$F(x; a_m, \beta_m) = \sum_{m=0}^{M} \beta_m f(x; a_m) \tag{1.21}$$

In this additive expansion, the classification function $F(x)$ depends on the weights of individual trees β_m and the parameters a_m of each individual tree. Boosting is used to adjust the parameters β_m and a_m so that the deviation between model response $F(x)$ and the true value y from the training sample, is minimized. Deviation between the classifier and the true value is described by the binomial log-likelihood loss-function $L(F(x), y) = \ln(1 + e^{-2F(x)y})$. Also other alternatives for the loss-function can be used, but the binomial log-likelihood loss-function performs well in noisy settings. Minimization of this function is done with the steepest-descent approach, as the boosting algorithm corresponding to this function is difficult to obtain. A resampling procedure using random subsamples of the training events for growing the trees is used to improve results, helping to stabilize the classifier. [28]

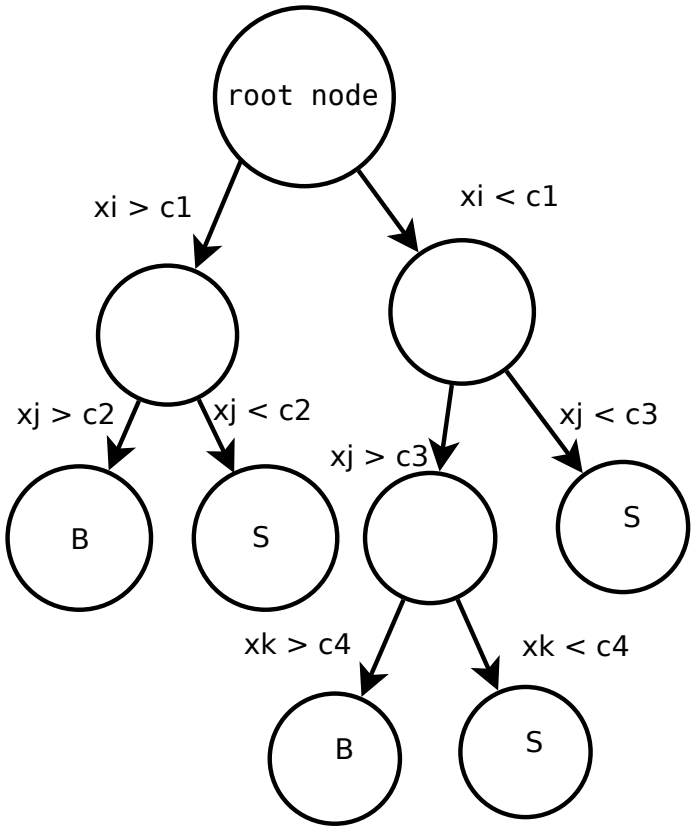

Figure 1.2: An example of a decision tree. Starting from the root node, several cuts ci on the training variables xi, xj and xk, are made. At each point, the variable and cut that give best separation between classes is used. In this example, the events are classified into signal (S) and background (B). [28]

1.4.2 Event weighting schemes

Once the classifier gives an estimate of the probability of an event to belong to a certain class, two different options can be used to determine how the event contributes to the observed fractions of classes in the sample. Each fraction is determined from the number of weighted events observed in each class over the total number of events classified. Event weights can be in the interval from zero to one per event and per class, with the sum of weights for all classes one for any single event, which corresponds to the requirement that each event has a probability of one to belong to any class.

Traditionally, the "hard" classification scheme is used; in this scheme the event is assumed to belong to the most probable class and therefore it counts as an event of aforementioned class (with weight one). In this scheme, as in the training step, the relative occurrences of signal and background class in the sample are assumed to be equal when determining the probability of belonging to a certain class, since the classifier itself gives a strong indication whether the event is signal or background like and unequal priors bias the classification.

In the "soft" classification scheme, the posterior probability of an event to belong to each class is determined and the event counts in each class with the weight determined by the probability. Different values for the prior probabilities can be used and often lead to different results. Sensitivity to priors can be reduced by using an iterative approach, in which the classification is performed repeated times, with the priors of the following step determined by the posterior probabilities of the current step.

Chapter 2

Experiment and accelerator

2.1 Accelerator

The construction of the Large Hadron Collider (LHC) at CERN was motivated by fundamental questions in particle physics, such as the question of the existence of the Higgs boson, and it was approved in December 1994 by the CERN Council. The LHC is the most powerful particle collider to date. The designed maximum centre-of-mass collision energy for proton-proton collisions is 14 TeV at a luminosity of 10^{34} $\mathrm{cm}^{-2}\mathrm{s}^{-1}$. The total event rate at maximum luminosity is at the order of 10^{9} s^{-1}. To deflect the 7 TeV proton beams (when running at maximum design energy), a magnetic field of 8.33 T is generated with superconducting magnets. The LHC can also be used to collide heavy ions at high energies. It is a two-ring hadron collider, 26.7 km long in circumference, using superconducting magnets. Two of the LHC experiments, CMS[29] and ATLAS[30], are general-purpose detectors designed for measurements at the highest luminosity, whereas TOTEM[15] is designed for measurements of forward physics at lower luminosities, LHCb[31] is specialized in b-quark physics and ALICE[32] in heavy ion physics. [33, 34]

The LHC is supplied with protons from the injection chain: Linac 2, Proton Synchrotron Booster (PSB), Proton Synchrotron (PS) and Super Proton Synchrotron (SPS) (Fig. 2.1).

The LHC consists of eight arc sections and eight straight sections, where the experiments and systems for machine operation reside. Due to lack of space, the LHC uses twin bore magnets instead of separate magnets for the two proton beams circulating in opposite directions. The beams cross at four interactions points. The LHC has 2808 bunches per proton beam and a nominal 25 ns bunch spacing. In normal running scenarios the beams do not collide head on, but with an angle of about $150 - 200$ μrad in order to avoid unwanted collisions near the interaction point. Luminosities of runs are not constant, but decay due to degradation of intensities and emittances of the beams, mainly due to the loss from collisions.

The LHC uses NbTi superconducting magnets, cooled down to a temperature of 2 K using superfluid helium, to operate fields above 8 T. The LHC accommodates

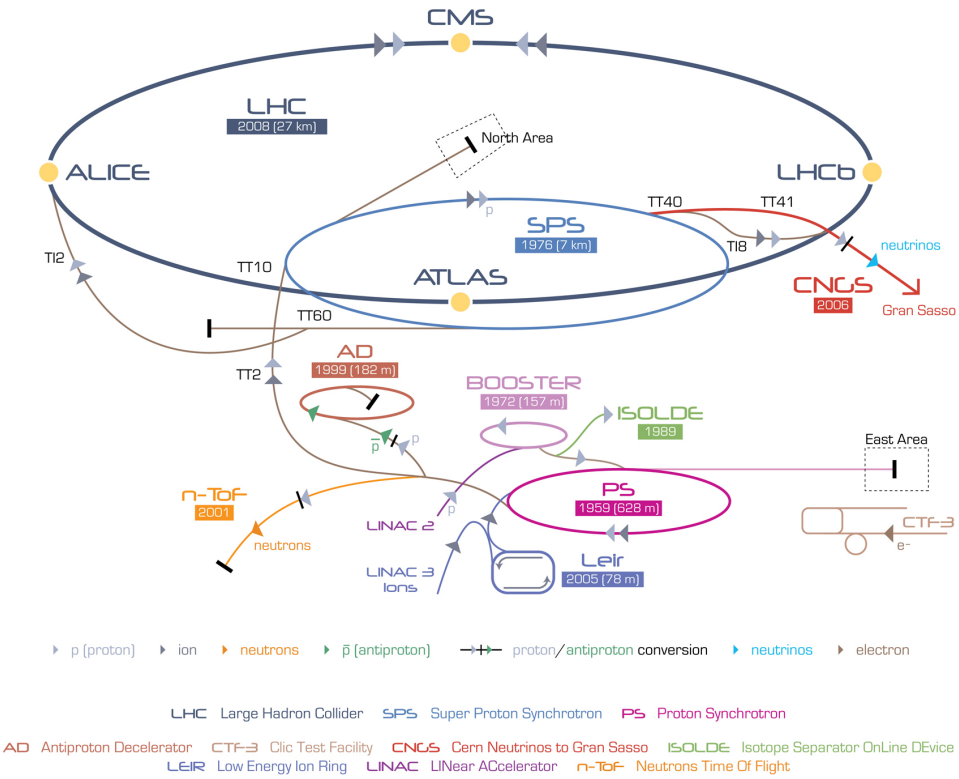

Figure 2.1: The LHC injector complex and the positioning of the four largest LHC experiments.[35]

1232 main dipole magnets, that are used for beam deflection. All of the main dipoles have practically identical characteristics; this is required in order to successfully operate the LHC. In addition to the dipoles there are the main quadrupole magnets for focusing and various corrector magnets (Octopoles, tuning quadrupoles, skew quadrupole correctors and combined sextupole-dipole correctors). Each of the LHC arcs consists of 23 regular cells, each having six dipole magnets and two quadrupole magnets.

The injection beam is captured, accelerated and stored using a 400 MHz superconducting cavity system. The RF accelerating systems provide a 16 MV voltage gradient at coast and 8 MV at injection.

The LHC has three vacuum systems: the insulation vacuum for cryomagnets, the insulation vacuum for helium redistribution and the beam vacuum. The equivalent hydrogen gas density in the beam vacuum needs to be below $10^{15} H_2\,\mathrm{m}^{-3}$ and $10^{13} H_2\ \mathrm{m}^{-3}$ around the experiments. The beam vacuum is divided into sectors, which most commonly correspond to the distance between two stand-alone cryomagnets. The LHC and its 1612 electrical circuits are powered via 3286 current leads.

While the LHC has been designed for a 14 TeV maximum center-of-mass collision energy, the accelerator has started off with lower beam energies. This has allowed to make sure everything works correctly before going to the higher energies. In addition, this has allowed for example cross-section measurements to be performed at various energies and study their energy dependence. The first collisions at the LHC in 2009 were at 900 GeV, and then the energy was raised to 2.36 TeV at the end of the year. In 2010 and 2011, the system was operated at 3.5 TeV per beam, totalling 7 TeV in collision energy (used in Sec. 4.1). A record high collision energy of 8 TeV was achieved in 2012 (used in Sec. 4.2 and Chapter 5). Before the end of LHC Run 1 in 2013, there was a time period of lower 2.76 TeV collisions (used in Sec. 4.3). After a two-year shutdown, the LHC started operating with 13 TeV collisions in 2015. [36]

2.2 Experiment

The TOTEM experiment is a small experiment at the LHC. It is dedicated to the measurement of the total proton-proton cross-section. This can be done with the luminosity-independent method, which is based on the Optical Theorem, and requires a measurement of the differential elastic scattering cross-section $d\sigma/dt$ down to a squared four-momentum transfer $|t|$ of $\sim 10^{-3}\,\mathrm{GeV}^2$ and the measurement of the total inelastic rate. Additional goals, aiming at a better understanding of the structure of the proton, include studies of elastic scattering over a wide $|t|$-range and diffractive processes. Some measurements are done together with the CMS experiment. The measurements done by TOTEM are complementary to those of the other LHC experiments; therefore whereas other experiments are mostly instrumented in the central region, TOTEM is instrumented in the forward region. TOTEM has two inelastic telescopes, T1 and T2, and Roman Pots, for detecting

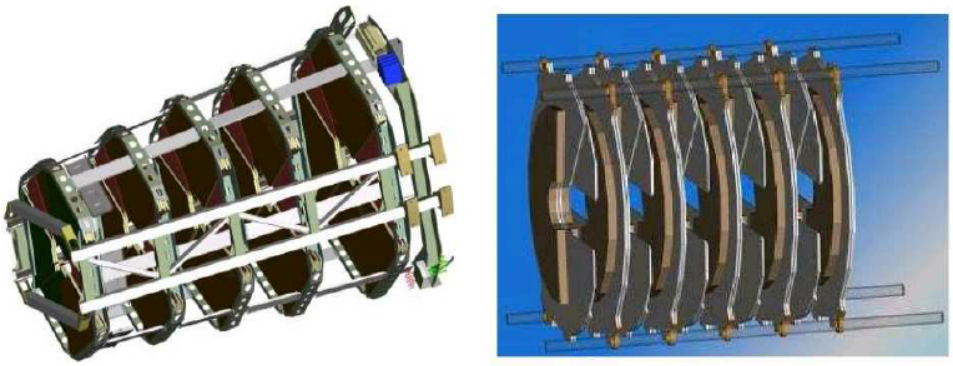

Figure 2.2: Drawings of one TOTEM T1 detector arm (left) and one T2 detector arm (right).[38]

leading protons, placed symmetrically around the interaction point (IP) at 147 and 220 m.[15]

T1 is centered at $\sim$ 9 m from the IP on both sides and consists of Cathode Strip Chambers (CSCs). It has 5 planes per arm, each composed of 6 CSCs and covers a pseudorapidity region $3.1 \leq |\eta| \leq 4.7$. The telescope arms are made of two vertically divided halves, half-planes, in order to enable installation around the beam pipe (Fig. 2.2 (left)). Each CSC covers 60° in azimuthal angle ϕ, with an overlap between adjacent CSCs. The CSCs contain an anode wire layer and two sets of cathodes at a 60° angle with respect to the anode direction. This configuration enables a 1 mm precision for the three coordinates for a particle track in a plane and allows to discriminate against noise from electronics.

T2 is in a symmetric two-arm configuration, with both arms centered at $\sim$ 13.5 m from the IP and uses Gaseous Electron Multipliers (GEMs). It is made of 20 half circular sectors of GEMs per arm, each of them covering 192° in ϕ, and covers a pseudorapidity range $5.3 \leq |\eta| \leq 6.5$ (Fig. 2.2 (right)). The chambers are read out through read-out boards with 256 strips for radial coordinate measurement and 1560 pads (in a configuration of 24 rows and 65 columns) for triggering and azimuthal coordinate measurement. The resolutions are 110 μm in the radial coordinate and 1° in ϕ. Advantages of the GEM technology include high rate capability, good spatial resolution, robust mechanical structure and excellent ageing properties. The readout of both T1 and T2 is based on VFAT front-end ASICs providing digital output signal and trigger [37]. The T2 trigger is based on groups of 3*5 pads, called super-pads. The trigger requirement of having at least one charged particle in any T2 half-arm is achieved by demanding signal in 4 or 5 super-pads in the same $r - \phi$ sector from different planes of the same T2 half-arm. The analyses presented in chapters 4 and 5 use events triggered by the T2.

The Roman Pots (RPs) are almost edgeless (the insensitive region at the edge

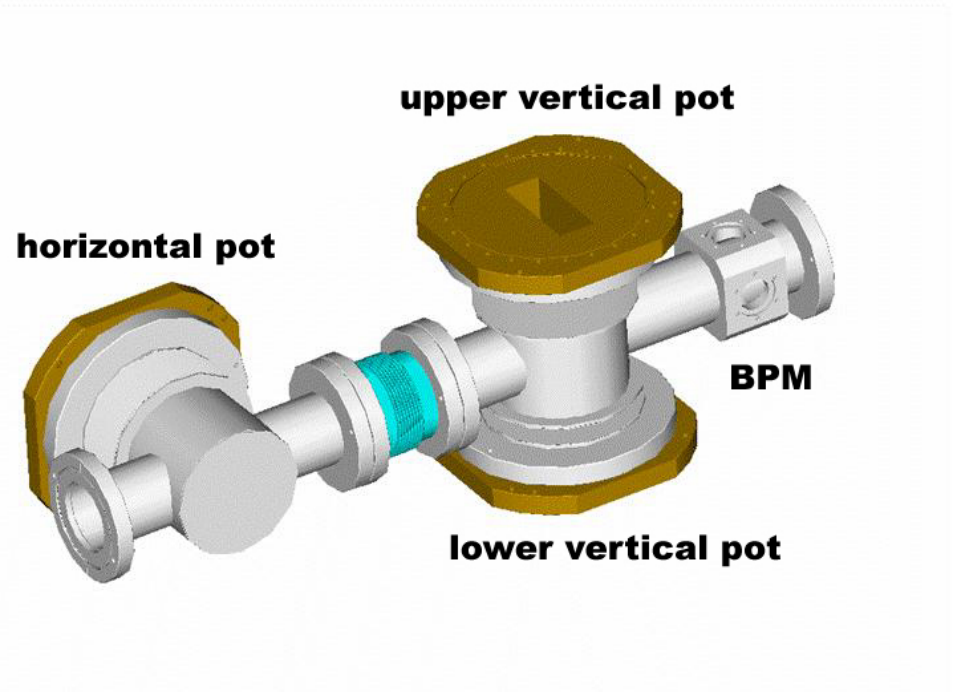

Figure 2.3: A Roman Pot unit.[15]

of the detector is only $\mathcal{O}(10\mu\text{m})$) silicon strip detectors placed in secondary vacuum vessels, which are moved into the primary LHC vacuum through vacuum bellows. The RP system is symmetric with respect to the IP and allows the reconstruction of protons on both sides of it. On each side of the IP, there are two stations of Roman Pots mounted on the beam pipe of the outgoing beam. Each station has two units and each unit has three pots; two approaching the beam vertically and one horizontally (Fig. 2.3). Each pot has 10 planes of edgeless silicon strip detectors. Half of the planes are at an angle of $-45°$ and the other half at $+45°$, a configuration that allows two-dimensional reconstruction.

TOTEM has a unique coverage for charged particles at high pseudorapidities and is therefore an ideal tool for studying forward physics. Thanks to the good forward coverage, at 8TeV center-of-mass collision energy $\sim 100\%$ of non-diffractive inelastic, $\sim 94\,\%$ of double diffractive and $\sim 83\,\%$ of single diffractive events can be seen, which corresponds to $\sim 95\,\%$ detection of all inelastic events.

Diffractive and elastic processes make up about half of the total cross-section. TOTEM is able to measure some of the protons from single diffraction and forward particles in single and double diffraction. Analyses of central diffraction can be done together with CMS; CMS has good coverage in the central region while TOTEM has the Roman Pot detectors for detecting the leading protons.

Chapter 3

Monte Carlo event generators

Monte Carlo event generators are used to simulate the interaction at the collision point and the results of the simulations are used to obtain certain corrections and e.g. for training the classifier in the classification analysis presented in this thesis (section 5). Event generators are based on different models, whose parameters are tuned to existing data.

The event generators PYTHIA 6[39, 40], PYTHIA 8[41] and PHOJET[42, 43] were used in some parts of the analyses. They allow the generation of different inelastic processes separately. All of them generate non-diffractive minimum bias, single diffractive and double diffractive events. PHOJET as well as the most recent versions of PYTHIA 8 also generate central diffractive events in addition to the previously mentioned ones.

Inclusive inelastic samples, containing all interactions described by the model, were also generated with QGSJET-II-03 and QGSJET-II-04 [10]. These generators do not allow to produce events separately via specific processes, but because their models significantly differ from the ones used in the other generators, they give a good indication of the model dependence of different quantities.

3.1 PYTHIA

PYTHIA 6 is a generator that produces complete events with the level of detail comparable with the experimentally observed ones. The full problem of event generation has been factorized in PYTHIA 6 into a number of components. The hard process is modelled, bremsstrahlung corrections are applied and the result is hadronized. Monte Carlo techniques are used to select all relevant variables according to the desired probability distributions. [39]

PYTHIA 8 comprises a set of physics models for the evolution from a few-body hard process to a complex multihadronic final state. It comprises a library of hard processes and models for initial- and final-state parton showers, multiple parton-parton interactions, beam remnants, string fragmentation and particle decays. The

physics models behind PYTHIA 8 are almost identical to the ones in PYTHIA 6. The full event generation problem is divided into a set of simpler separate tasks, just like in PYTHIA 6. Since all the main aspects of the event are generated, the results from PYTHIA 8 are comparable with those from experimental data. [41]

Total, elastic and inelastic cross-sections in PYTHIA are obtained from Regge fits. In the case of proton-proton-interactions, the 1992 Donnachie-Landshoff parametrization[44], with one Pomeron and one Reggeon term, is used;

$$\sigma_{\mathrm{tot}}^{\mathrm{pp}}(s) = 21.70 s^{0.0808} + 56.08 s^{-0.4525}\,\mathrm{mb}, \tag{3.1}$$

with s in GeV^2. In the case of the elastic cross-section, a simple exponential falloff with momentum transfer t, is assumed. It is related to the total cross-section via the optical theorem. The inelastic cross-section is then obtained as the difference of the total and elastic cross-sections. Modelling of hard physics processes is based on a factorized picture of perturbative matrix elements, combined with initial- and final-state parton showers and the Lund string hadronization model[45]. In multi-parton-interaction (MPI) models this picture can be extended to cover soft transverse momentum scales via the introduction of an infrared regularization scale. MPI is used for the modelling of all inelastic non-diffractive events in PYTHIA.

In PYTHIA 6, diffractive events are treated as purely non-perturbative, with no partonic substructure. A diffractive mass M_{X} is selected and the final state is produced by modeling the diffractively excited system as a single hadronizing string with invariant mass M_{X}. PYTHIA 8 handles soft diffraction the same way as PYTHIA 6, but the default modeling of hard diffraction[46] follows an Ingelman-Schlein approach[47] to introduce partonic sub-structure in high mass events.

In the inelastic event classification analysis, the MBR (Minimum Bias Rockefeller) model[48] of diffraction, which is implemented in PYTHIA 8, is used in addition to the usual PYTHIA 8 model. This model follows renormalized Regge theory and has been tested on CDF data. Treatment of non-diffractive and elastic events is not changed by the model.

There are multiple tunes of PYTHIA 8 and two of them were used in the analyses included in this thesis. PYTHIA 8-4C[49] is tuned to early LHC data, while the newer PYTHIA 8 Monash 2013[50] is tuned to more recent LHC data (up to 8 TeV).

3.2 PHOJET

PHOJET is an event generator, whose model is based on the Dual Parton Model[51] combined with perturbative QCD. Both elastic and inelastic processes can be modelled within the Dual Parton Model. This model is closely related to the Quark-Gluon-String Model[52]. The PHOJET model uses a two-component scheme with a soft and a hard component. The model is self-consistent for all partial cross-sections and includes interplay of soft, hard, diffractive and non-diffractive interactions. The calculations in PHOJET start with amplitude calculations and then physical cross-sections are calculated by unitarizing the Born amplitudes, with the

elastic scattering amplitude being constructed from the sum of soft and hard interactions using the optical theorem. The model treats charm quarks as massless and the heavier quarks are not included in calculations. Unknown model parameters are obtained by comparing the model predictions with cross-section data.[53]

The first step of modeling of inelastic states is the calculation of cross-sections for different inelastic states (diffractive and non-diffractive). In the model, the sizes of diffractive cross-sections are directly linked to multiplicities in non-diffractive interactions, which leads to strong model constraints. The partonic color flow of each event is sampled explicitly in the limit of large number of colours N_C.[54] Partons are combined to color-neutral strings and PYTHIA 6 is used to generate final state radiation for hard interactions and for string fragmentation and hadronization. A prediction of the PHOJET model is that the increase of the mass/energy of the pseudorapidity plateau of charged particles in diffractive interactions is similar or faster to that of non-diffractive interactions[55]. None of the versions of PHOJET are tuned to LHC data.

3.3 QGSJET

QGSJET has been developed for and mainly used by different groups in high energy cosmic ray physics. Experimental measurements of high energy cosmic rays (energies above 10^{14} eV) are based on an indirect method, where properties of primary particles are reconstructed from properties of extensive air showers (EAS) induced by the cosmic rays in the atmosphere. The quality of the data depends heavily on the understanding of EAS physics. Current versions of QGSJET can treat nucleus-nucleus interactions, such as proton-proton, and semihard processes. The QGSJET model treats collisions in the framework of Gribov's reggeon approach [56, 57]. It includes realistic nuclear density parametrizations and two-component treatment of low mass diffraction. Accelerator data has been used to calibrate the parameters. [10]

The model[58, 59] is based on the Reggeon Field Theory (RFT) framework. The physics picture is that of multiple scattering processes: the interaction is mediated by multiple parton cascades developing between projectile and target. In the RFT such cascades are represented by pomerons, which are composite objects with vacuum quantum numbers. To be compatible with perturbative QCD, the "semihard pomeron" scheme, is used. The parton evolution is described in the region of relatively high virtualities using the DGLAP formalism and using phenomenological soft pomeron amplitude for non-perturbative parton cascades[60]. The RFT scheme is based on the "general pomeron", which is the sum of soft and semihard ones.

This scheme allows to develop a coherent framework for calculations of total and elastic cross-sections for hadron-hadron scattering and for derivation of partial cross-sections for various inelastic final states, including the diffractive ones [61]. The optical theorem and the AGK (Abramovskii, Gribov and Kancheli) cutting rules are applied. Use of the cutting rules allows calculation of partial cross-sections

for all possible final states by considering unitarity cuts of various elastic scattering diagrams. QGSJET-II-04 is tuned to early LHC data [62].

3.4 Remarks

The use of multiple generators for calculating various corrections and expected particle distributions allows to quantify the amount of model dependence in the analyses.

Some of the output of the generators can be directly compared with data. For instance the fraction of single-sided events in T2, meaning events with particle tracks observed only on one side of the interaction point in the T2 detector, is easily measured and compared. Such events are typically single diffractive. Based on the TOTEM measurements, the QGSJET-II-03 generator is much closer to the data than the other generators in this regard. This quantity is mostly determined by the relative fractions of single diffractive events in the full inelastic cross-section as well as by the diffractive mass spectrum used.

On the other hand, other properties, such as particle multiplicities, are better described by PYTHIA 8 for which several LHC tunes exist. None of the generators describe all aspects of the inelastic collisions perfectly.

Chapter 4

Inelastic cross-section measurements

In this chapter the inelastic pp cross-section measurements are presented in the order the analyses were made.

4.1 Measurement at 7 TeV

The inelastic cross-section at $\sqrt{s} = 7\,\text{TeV}$ had been previously measured by ALICE [63], ATLAS[64] and CMS[65]. These experiments have limited forward acceptance and therefore they can measure the majority of non-diffractive interactions, but only a limited range of diffractive masses for diffractive processes. The diffractive mass (M_X) coverage of an experiment depends on the maximal $|\eta|$ coverage of the detectors. The TOTEM measurement had a mass coverage down to $M_\text{X} \geq 3.4\,\text{GeV}$ ($|\eta| \leq 6.5$), whereas the others had $M_\text{X} \geq 7.0\,\text{GeV}$ (ALICE with $|\eta| \leq 5.1$) at best. The fraction of events beyond the instrumented regions were estimated in all analyses using phenomenological models. In the present analysis the model dependence was very low thanks to the good coverage, with $\sim 95\,\%$ of all inelastic events seen. [66]

The measurement was based on $\mathcal{L} \approx 82.8\,\mu\text{b}^{-1}$ of pp collisions at $\sqrt{s} = 7\,\text{TeV}$ recorded in October 2011 during a special $\beta^* = 90\,\text{m}$ optics fill with low inelastic pile-up ($\sim 3\%$). For this analysis, events triggered by T2 or from a zero-bias trigger stream were used. The data was analyzed divided into 5 different subsets in time in order to see time-dependent effects.

The observed inelastic rate was derived from the rate of events triggered by T2. Several corrections were applied, in three steps, to obtain the true inelastic rate. The full list of corrections is summarized at the end of this chapter in Tab. 4.1 together with the values from all the measurements presented in this chapter.

Corrections in the first step led to the inelastic rate for events with at least one particle in the T2 acceptance. After the second step, the rate for events with at

least one particle with the pseudorapidity $|\eta| \leq 6.5$ was obtained. The third and final step led to the full inelastic cross-section.

The events were divided into three categories: events with tracks in both T2 hemispheres ("2h events", dominated by non-diffractive minimum bias and double diffraction), events with tracks in only the positive hemisphere ("1h+ events", dominated by single diffraction) and events with tracks in only the negative one ("1h- events", also dominated by single diffraction). This categorization was used due to different trigger efficiencies and beam gas background contributions in the different categories.

The corrections for obtaining the rate of events with at least one charged particle in the T2 acceptance ("T2 visible") were the beam-gas background correction, trigger inefficiency correction, pile-up correction and the T2 reconstruction inefficiency correction. The beam-gas background correction, which only affects "1h events" due to its fixed-target nature, was determined from events triggered by non-colliding bunches. On the overall rate it was a 0.6 % correction. The trigger inefficiency correction was determined from the zero-bias data as a function of T2 track multiplicity. It is the most significant for events with one or few tracks and essentially zero for events with 10 tracks or more. The correction on the overall rate was 2.3 %.

The pile-up correction was estimated from zero-bias data using Poisson statistics. The correction on the overall rate was 1.5 %.

The T2 reconstruction inefficiency was estimated using three Monte Carlo event generators: PYTHIA 8, PHOJET and QGSJET-II-03. Additional scaling was used to correct the fraction of "1h events" to match the data. The correction, which represents the fraction of events with produced particles, but no tracks in the T2 acceptance, was 1.0 %.

Because T1 was not used for triggering, the fraction of "T1 only events", with particles in the T1 acceptance, but not in that of T2, was determined from zero-bias data and corresponded to a 1.6 % correction. Since a part of these events were recovered by the T2 reconstruction inefficiency correction, 0.5 % was subtracted to avoid double counting.

A correction of 0.35 % was applied to account for events that have an internal rapidity gap over a T2 arm and no particles produced in the other T2 arm or T1. The fraction of events that have all final state particles produced at $|\eta| > 6.5$, but due to secondaries are seen in T2, was estimated from the QGSJET-II-03 event generator; this gave a 0.4 % correction that was subtracted. The remaining events with all final state particles produced at $|\eta| > 6.5$ gave a 4.2 % correction to the full inelastic rate.

The cross-section for events with at least one final state particle in the pseudorapidity region $|\eta| \leq 6.5$ was measured to be 70.5 ± 2.9 mb, while the total inelastic cross-section was obtained as 73.7 ± 3.4 mb based on models for low mass diffraction. An upper limit on the amount of low mass diffraction (masses below 3.4 GeV, corresponding to events with all final state particles above the upper edge of the T2 acceptance $|\eta| > 6.5$) of 6.31 mb was obtained at 95% confidence level from the difference between the total inelastic cross-section obtained by TOTEM from

a measurement using only elastic scattering, $\sigma_{\text{inel}} = 73.15 \pm 1.26$ mb [67], and the directly measured $|\eta| \leq 6.5$ inelastic cross-section. At 68.3% confidence level the result was $\sigma_{\text{inel},|\eta|>6.5} = 2.62 \pm 2.17$ mb. [66]

The inelastic rate obtained was also combined with the elastic measurement to obtain the luminosity independent measurement, which gave a compatible result $\sigma_{\text{inel}} = 72.9 \pm 1.5$ mb.[68]

4.2 Measurement at 8 TeV

The cross-section measurement was redone at 8 TeV collision energy [69]. Having dedicated LHC beam optics (two fills recorded in July, 2012 with $\beta^* = 90$ m optics) and the Roman Pot detectors very close to the beam, enabled detection of $\sim 90\%$ of elastic events while the T1 and T2 telescopes simultaneously detected the majority of inelastic events. The total cross-section was measured using the luminosity-independent method (equation 1.18), $\sigma_{\text{tot}} = 101.7 \pm 2.9$ mb, and the inelastic cross-section, $\sigma_{\text{inel}} = 74.7 \pm 1.7$ mb, was inferred from it. The analysis procedure for the inelastic rate measurement was equivalent to the one used for the 7 TeV inelastic cross-section measurement (section 4.1).

4.3 Measurement at 2.76 TeV

Preliminary results of the inelastic cross-section measurement at $\sqrt{s} = 2.76$ TeV are presented in this section [70]. The measurement at 2.76 TeV followed the same idea as the previous measurements at 7 and 8 TeV (sections 4.1 and 4.2). The data for the analysis was recorded in 2013 in a run with special $\beta^* = 11$ m optics.

Due to limited statistics in the zero bias sample, the trigger inefficiency correction was slightly modified from the earlier measurements. The correction was now done per event category ("2h events", "1h+ events" and "1h- events"), but integrated over multiplicity, because the statistical fluctuations in the efficiencies as a function of track multiplicity in T2 were too large. An independent estimate of the trigger efficiency was done applying the trigger algorithm on the T2 pad data to mimic the electronic trigger. The systematic uncertainty was evaluated by adding the difference between the correction to the overall inelastic rate due to the two trigger efficiency estimates and the variation required on the 1h trigger efficiency of each method to give compatible fractions for left and right arm. For the 2.76 TeV analysis also the loss due to central diffractive events with all particles either $|\eta| > 6.5$ or more central than T1 was regarded to be large enough that it required a correction and not only a systematic uncertainty as in the 7 and 8 TeV analysis.

The preliminary result obtained for the inelastic cross-section using the luminosity independent method at this energy was $\sigma_{\text{inel}} = 62.8 \pm 2.9$ mb, after taking into account all the corrections.

4.4 Summary of cross-section measurements

The inelastic cross-sections obtained in the analyses presented in this chapter were $\sigma_{\text{inel}} = 62.8 \pm 2.9\,\text{mb}$ at 2.76 TeV, $\sigma_{\text{inel}} = 73.7 \pm 3.4\,\text{mb}$ and $\sigma_{\text{inel}} = 72.9 \pm 1.5\,\text{mb}$ at 7 TeV (luminosity dependent and independent, respectively), $\sigma_{\text{inel}} = 74.7 \pm 1.7\,\text{mb}$ at 8 TeV. Corrections and their uncertainties are summarized in Tab. 4.1.

Pile-up is different in the different analyses due to different beam intensities and highest at 2.76 TeV with $\beta^* = 11\,\text{m}$ optics. The beam gas background correction is of similar order in the 7 and 8 TeV measurements, but smaller in the 2.76 TeV thanks to the higher pileup since the beam gas background scales with the beam intensity and the pile-up with the beam intensity squared. Trigger inefficiency is higher in the 7 TeV analysis than the other two, since the trigger of T2 was improved with time. Event reconstruction efficiency and "T1 only" fractions are of similar magnitude in all analyses. The relative amount of the low mass diffraction correction increases with energy since the mass range not observed increases also, from $M_X \leq 2.1\,\text{GeV}$ at 2.76 TeV to $M_X \leq 3.4\,\text{GeV}$ at 7 TeV and $M_X \leq 3.6\,\text{GeV}$ at 8 TeV.

	2.76 TeV		7 TeV		8 TeV		
Source	Corr. [%]	Unc. [%]	Corr. [%]	Unc. [%]	Corr. [%]	Unc. [%]	Effect on
Beam gas	0.10	0.10	0.60	0.40	0.45	0.45	all rates
Trigger efficiency	1.2	0.8	2.3	0.7	1.2	0.6	all rates
Pile up	5.5	0.7	1.5	0.4	2.8	0.6	all rates
T2 event reconstruction	0.6 (0.9)	0.3 (0.45)	0.5 (1.0)	0.25 (0.5)	0.35 (0.8)	0.2 (0.4)	N_{inel}, $N_{\lvert\eta\rvert<6:5}$ (N_{T2vis})
T1 only	1.6	0.4	1.6	0.4	1.2	0.4	N_{inel}, $N_{\lvert\eta\rvert<6:5}$
Central diffraction	0.60	0.50	0.00	0.35	0.00	0.35	N_{inel}, $N_{\lvert\eta\rvert<6:5}$
Internal gap covering T2	0	0.30	0.35	0.15	0.40	0.20	N_{inel}, $N_{\lvert\eta\rvert<6:5}$
Low mass diffraction	3.1 (0.3)	1.6 (0.15)	4.2 (0.4)	2.1 (0.2)	4.8 (0.4)	2.4 (0.2)	N_{inel} ($N_{\lvert\eta\rvert<6:5}$)

Table 4.1: Corrections of the different cross-section measurements and their uncertainties.

Chapter 5

Classification of inelastic events

The relative contributions of diffractive and non-diffractive processes to the inelastic cross-section are not well understood, since they cannot be calculated with perturbative QCD. Measurements are needed to understand these fractions, since the currently existing models cannot give consistent and reliable estimates. In this analysis, the fractions and process-specific cross-sections of non-diffractive, single diffractive and double diffractive processes (σ_{ND}, σ_{SD} and σ_{DD}), which are the largest contributions to the inelastic cross-section, were determined using a multivariate analysis method based on boosted decision trees[24]. The previously measured inclusive inelastic cross-section σ_{inel}[69] was used as the normalization and combined CMS and TOTEM data from the same fill was used in the analysis. Classification was done for the T2 visible cross-sections and then corrected for acceptance.

The analysis was based on certain key variables of the events, which have different distributions depending on the event category. Multivariate methods for classification of events at the LHC had been proposed and used previously on simulated samples [71, 72]. Here classification using multivariate methods was taken a step further using measured data for the final determination of the fractions. A similar measurement has been done at Fermilab with the CDF-detector at $\sqrt{\mathrm{s}} = 1.96$ TeV [73].This is a very original method compared to previous literature on diffractive cross-section measurements.

The classifier used analysis variables calculated from quantities measured in the CMS and TOTEM detectors with different distributions depending on event class. Central diffraction, whose cross-section is expected to be a minor fraction of the inelastic cross-section ($\sim 1\,\%$) and an order of magnitude smaller than the single and double diffractive ones, was not included in the current analysis. The inelastic event sample was represented by events having tracks in T2 vetoing events with two reconstructed protons in the RPs in order to reject elastic background. Based on studies of central diffractive events generated with PYTHIA 8 with MBR model for diffraction [48], about half of the central diffractive events are suppressed by these requirements and the remaining central diffractive contribution would be included

mostly in the single diffractive cross-section in this analysis.

Since events produced via the different processes by the generator in many cases have identical-looking final states, an experimental definition of the different processes based on the generator level particles was used instead of the class given by the Monte Carlo model. This definition was derived from the fact that diffractive events are expected in the majority of cases to have a clear rapidity gap, that is, a region in pseudorapidity space in which no final state particles are produced. This also makes comparisons to earlier rapidity gap based analyses possible. Events with a proton at the highest or lowest pseudorapidity followed by a gap of $\Delta\eta \geq 3$ units in pseudorapidity were considered single diffractive, with separate classes for events with the dissociated system on the right and left sides (SDR (Fig. 5.1a) and SDL (Fig. 5.1b), respectively). If there were generated protons at both lowest and highest pseudorapidity and both were followed by a gap of $\Delta\eta \geq 3$, the side with the larger gap was considered the side of the forward proton. Other events, where the largest rapidity gap was $\Delta\eta \geq 3$ were considered double diffractive (DD (Fig. 5.1c)) and all other events non-diffractive (ND (Fig. 5.1d)). This definition agrees with the recommendation of the LHC Minimum-bias and underlying event working group [74].

In practice, the analysis was done using gradient boosted decision tree (BDTG) classifiers of the TMVA toolkit[28, 75]. The binarization of the multiclass problem was done manually using ordered binarization: in the first classifier the probability that the event was non-diffractive P_{ND} was determined, in the second the probability that it was one of the single diffractive configurations $P_{\mathrm{SDL(R)}}$ and in the third and last classifier the probability that it was the other single diffractive configuration $P_{\mathrm{SDR(L)}}$ or double diffractive P_{DD}. The sum of all probabilities for each event was one, which means that after each step, the amount of probability left for the remaining classes was reduced by the probability assigned to the signal class. Both choices for the single diffractive process to be treated in the second step were done and the final result was taken as an average of the two paths. Classifiers were also trained and used in the reverse order to check for any bias introduced by the order of binarization. While such an order was suboptimal, since the classification performs best when the class with best separation is eliminated first, the result was compatible with the one obtained with optimal ordering.

Features that distinguish the different event types from each other include particle multiplicities, how the particles are distributed in pseudorapidity and whether or not they have final state protons at very forward angles on either side of the interaction point. The detectors used for the analysis were the Roman Pots and T2 from TOTEM and the CMS subdetectors in the central region. The TOTEM T1 detector was not used, because it was running at lower voltage, leading to a reduced efficiency, in order to protect the CSCs from the high amount of radiation resulting from the high event rate. Similarly the FSC detectors from CMS were not used, because their efficiencies were not fully understood at the time of analysis. In the CMS region the particle flow[76, 77] objects were used. These objects were constructed by the particle flow algorithm, which combines information from all the subdetectors to reconstruct the final state particles' properties. The full set of

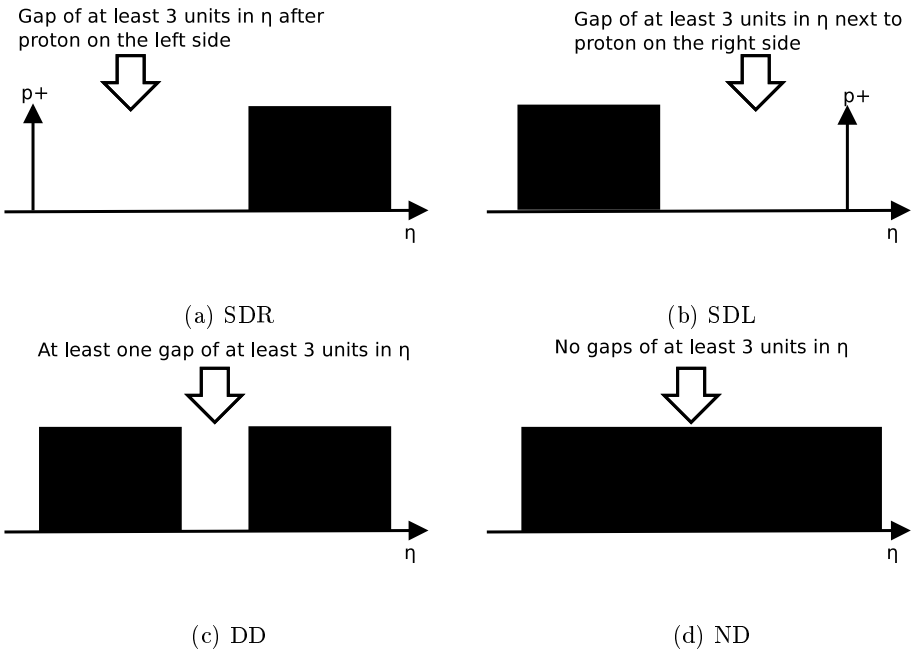

(a) SDR

(b) SDL

(c) DD

(d) ND

Figure 5.1: Rapidity gap based definitions of generated event classes. SD right and left convention is based on the side of the diffractive system.

Variable	Description
$\Delta\eta$	Largest gap in η between any two adjacent reconstructed T2 particles or particle flow objects in the event (excluding RP protons), assuming acceptance gaps between detectors to contain no particles
$\eta_{\min}$ and $\eta_{\max}$	Smallest and largest η of reconstructed T2 particles or particle flow objects in the event (excluding RP protons)
$N_{\mathrm{T2}+}$ and $N_{\mathrm{T2}-}$	Reconstructed particle multiplicity in T2 "+" and "−"-arm
N_{CMS}	Reconstructed multiplicity of CMS particle flow objects
ξ_{left} and ξ_{right}	Reconstructed momentum loss ξ of proton (if any) on left and right side of IP5, otherwise -1

Table 5.1: The variables used for classification.

variables is listed and described in Table 5.1. Samples simulated with PYHIA8-4C were used for training the classifiers used in the analysis. Because the training events were generated without pile-up, the effects of pile-up were added to the simulation by combining the generated events with random events from zero-bias data recorded at the same time as the minimum bias triggered events used for the rest of the analysis. This way of taking the pile-up into account was systematically done throughout the analysis. Distributions of the variables, separately for the training samples of different classes (ND, DD, SDL and SDR) are shown in Fig. 5.2. These distributions give indications of how the different variables will be used to separate the different classes.

In addition to the training events produced with P8-4C, separate inclusive inelastic samples were produced with P8-4C, QGSJET-II-04 (QGSJET)[10], PYTHIA 8-4C tune with MBR model for diffraction (P8-MBR)[48] and PYTHIA8 with the latest Monash 2013 tune (P8-Monash)[50]. These were used to test the classification, cross-check results and to estimate systematic uncertainties.

The data sample used for the final classification step was recorded by both CMS and TOTEM, in July 2012, in a dedicated run with 8 TeV p-p collisions with low pile-up probability (mean of Poisson distribution $\mu \sim 4.4\,\%$) and special $\beta^* = 90\,\mathrm{m}$ optics, where β^* is the amplitude function of the beam at the interaction point. A minimum bias trigger, provided by the TOTEM T2 detector, contributed to the CMS global trigger decision, which initiated simultaneous readout of both the CMS and TOTEM detectors. The CMS orbit-counter reset signal delivered to the TOTEM electronics at the beginning of each run ensured time synchronization of the two experiments. The data from both experiments was later combined to a common sample by matching events using bunch and LHC orbit numbers. The minimum bias trigger required at least one track candidate in the T2 detector. Zero bias data was triggered on random bunch crossings and allowed the study of pile-up and noise effects. This joint effort allowed us to perform the classification with an extensive set of detectors and with a good acceptance in the pseudorapidity phase space.

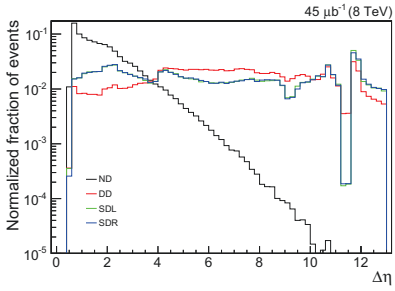

(a) Reconstructed maximum rapidity gap

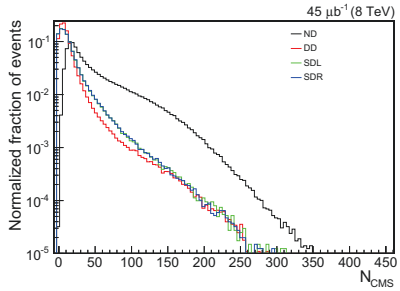

(b) CMS multiplicity

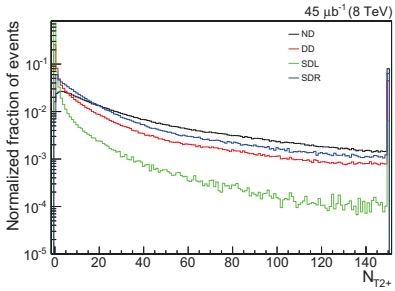

(c) T2+ multiplicity

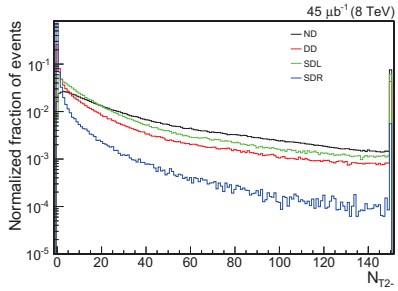

(d) T2- multiplicity

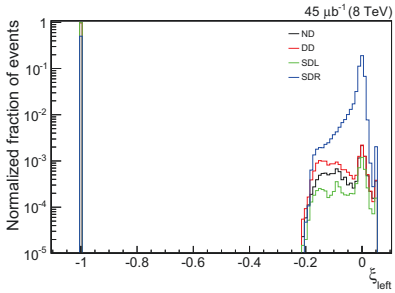

(e) Proton ξ_{left}

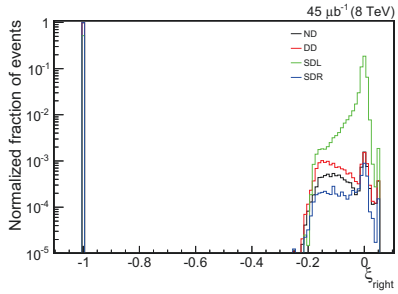

(f) Proton ξ_{right}

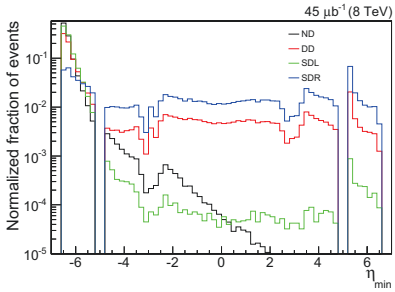

(g) η_{min}

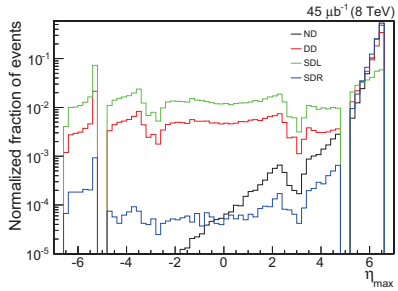

(h) η_{max}

Figure 5.2: Distributions of classification variables in the different training samples. All simulated samples include mixing with random zero-bias events to take into account the effect of pile-up.

	Step 1	Step 2		Step 3		
	ND	SDL	SDR	SDR	SDL	Nvar
Global	0.868	0.797	0.800	0.677	0.671	8
Local CMS	0.600	0.356	0.356	0.273	0.271	4
Local CMS+T2	0.789	0.632	0.625	0.381	0.384	12
Local CMS+T2+RP	0.875	0.798	0.800	0.680	0.673	14

Table 5.2: The signal efficiency at 10 % background efficiency for the different subsets of variables (see text for definition) at the different classification steps based on the PYTHIA 8-4C training sample. The total number of variables in each subset is shown under Nvar.

The signal efficiencies, when accepting 10 % background contamination from other classes for the different subsets of variables are shown in Table 5.2. This is a figure of merit of the classifier, giving the efficiency at 90 % purity. For the local subset also $\Delta\eta$, $\eta_{\min}$ and $\eta_{\max}$ are defined locally i.e. within either CMS or T2. Based on these results, the global subset gave a classification performance comparable to that of the full local subset with less variables and therefore it was chosen as the set of variables to be used in the reported analysis. The difference between different local subsets clearly shows the added value both T2 and RPs give to the classification.

Distributions of the classification variables in the inelastic event samples, with relative contributions from different processes set at the default values for each tune, can be seen in Fig. 5.3 along with the distributions for data. With the exception of the first few bins in all of the multiplicity plots, the agreement between the different simulated samples and data is good in these variables and in all cases except for the proton momentum losses, P8-4C is the closest match. For the proton momentum losses, the QGSJET sample and the data show better agreement. The $\Delta\eta$, $\eta_{\min}$ and $\eta_{\max}$ distributions are dependent on the relative fractions of diffraction in the sample and also sensitive to the model of diffraction. Therefore complete agreement in these variables between data and simulation is not necessarily expected. Events with $\eta_{\min}$ or $\eta_{\max}$ in the CMS Hadron Forward (HF) calorimeter region ($3.2 \leq |\eta| \leq 4.7$) are more abundant in the data compared to simulation. The most common type of such event has a rapidity gap over one of the T2 arms or only neutral particles in the region, since T2 can only detect charged ones, but no major gaps elsewhere in the event and hence show up in the HF region in $\eta_{\min}$ or $\eta_{\max}$ distributions.

The results of the raw relative fractions, e.g. the fractions in the T2-triggered sample prior to acceptance corrections, for the five different samples, PYTHIA 8-4C (P8-4C, different samples from same generator used for training), QGSJET-II-04 (QGSJET), PYTHIA 8-4C with MBR model of diffraction (P8-MBR), PYTHIA 8-Monash 2013 (P8-Monash) and data, are shown in Table 5.3. Classification was performed using different methods and priors. Hard classification assigned each event to the most probable class, while the other methods were soft: each event

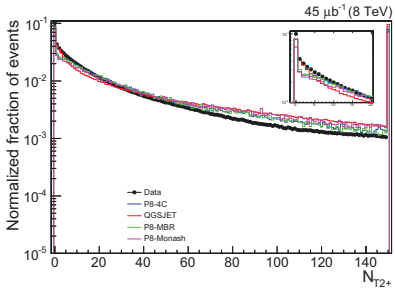

(a) T2+ multiplicity

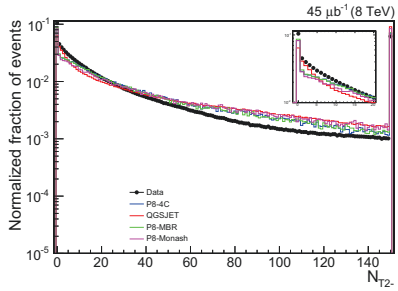

(b) T2- multiplicity

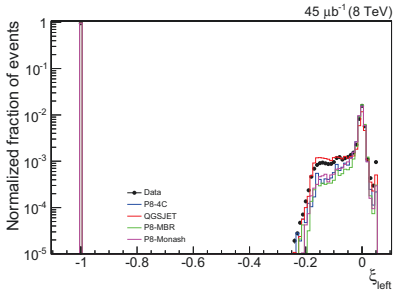

(c) Proton ξ_{left}

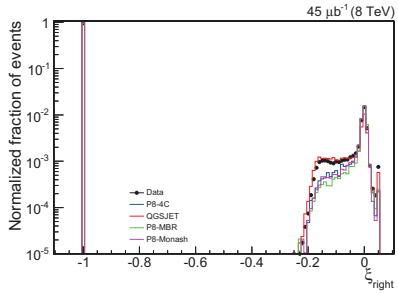

(d) Proton ξ_{right}

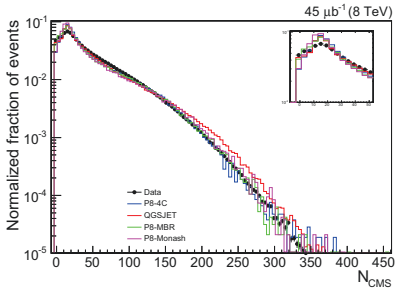

(e) CMS multiplicity

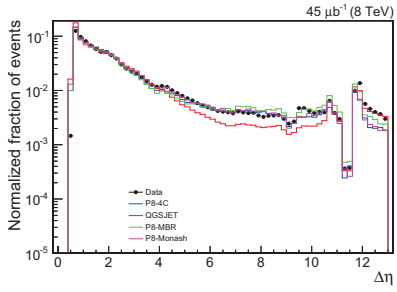

(f) Reconstructed maximum rapidity gap

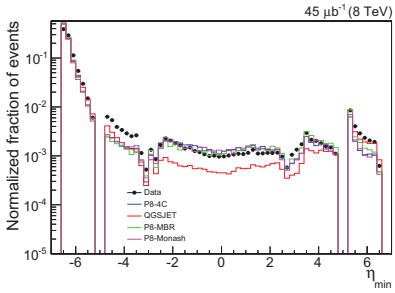

(g) η_{min}

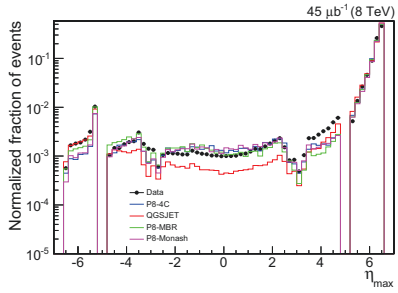

(h) η_{max}

Figure 5.3: Distributions of classification variables in the inelastic data and MC samples with relative weights of different processes at their default values for the MCs. All simulated samples include mixing with random zero-bias events to take into account the effect of pile-up.

	P8-4C		QGSJET		P8-MBR		P8-Monash		Data	
	Exp.	Bias	Exp.	Obt.-Exp.	Exp.	Obt.-Exp.	Exp.	Obt.-Exp.	Obt.	Unc.
					Hard					
ND	0.755	1.020	0.756	0.025	0.746	-0.005	0.753	-0.002	0.700	0.026
SDL	0.074	0.903	0.084	-0.012	0.068	0.007	0.073	0.001	0.092	0.012
SDR	0.074	0.874	0.084	-0.012	0.069	0.005	0.073	0.001	0.094	0.014
DD	0.097	1.039	0.076	-0.002	0.117	-0.007	0.100	0.000	0.114	0.009
					P8					
ND	0.755	0.991	0.756	0.035	0.746	-0.006	0.753	0.000	0.707	0.036
SDL	0.074	0.980	0.084	-0.017	0.068	0.006	0.073	0.000	0.087	0.017
SDR	0.074	0.972	0.084	-0.017	0.069	0.005	0.073	0.000	0.090	0.017
DD	0.097	1.120	0.076	-0.001	0.117	-0.005	0.100	0.001	0.116	0.008
					Iter.					
ND	0.755	0.989	0.756	0.049	0.746	-0.012	0.753	-0.002	0.688	0.050
SDL	0.074	0.967	0.084	-0.019	0.068	0.006	0.073	0.000	0.092	0.019
SDR	0.074	0.956	0.084	-0.019	0.069	0.004	0.073	-0.001	0.095	0.020
DD	0.097	1.175	0.076	-0.011	0.117	0.002	0.100	0.003	0.125	0.014

Table 5.3: The expected raw fractions (Exp.) based on generator-level information and the differences between the raw fractions determined by the classifier and expectation (Obt.-Exp.), which have been corrected for the bias (Bias) as observed in the P8-4C sample, for the different simulated samples, weighting schemes and priors (hard, soft with P8-4C priors (P8) and iterative with equal priors (Iter.)) as well as the obtained fractions for data and their uncertainties (Unc.).

got a weight to belong to each class, which was determined by the probability of belonging to the class as given by the classifier. The probability of belonging to each class is dependent on the prior probabilities of the classes and therefore different prior probabilities were considered. In the result labelled "P8", the prior probabilities are represented by the relative cross-sections of each process in P8-4C. In "Iter.", each process is assigned equal prior probabilities to begin with and the classification is performed several times, starting with the posterior probabilities from the previous iteration as new priors, until equilibrium is reached. Several different starting priors were tested for the iterative method (equal, default fractions in P8-4C as well as 40 % ND, 30 % DD and 15 % of both SD classes) and the same result was obtained independent of the choice of starting priors. A classification bias correction was applied to each event class based on the ratio of the expected and observed fractions in P8-4C, since this was the model used for training. The systematic uncertainties of the classification method were estimated by comparing the expected and obtained fractions for all the Monte Carlo samples within each event weighting scheme and within each event class. The full systematic uncertainty of the raw data fractions was obtained from the quadratic sum of half of the bias correction and the full method uncertainty.

The hard weighting scheme was chosen for the final result, since it gave consistently good results for all the Monte Carlo samples and the combinations of the method and bias uncertainties were smallest, therefore leading to the smallest systematic uncertainties.

Different event classes have different probabilities to be inside the T2 acceptance

	P8-4C		QGSJET		P8-MBR		P8-Monash	
	Acc.	Low M_X	Acc.	Low M_X	Acc.	Low M_X	Acc.	Low M_X
ND	1.00	1.00	1.00	1.00	1.00	1.00	1.00	1.00
SDL	0.83	0.84	0.75	0.78	0.80	0.84	0.84	0.85
SDR	0.83	0.84	0.75	0.78	0.80	0.84	0.84	0.85
DD	0.94	0.95	0.95	0.97	0.96	0.96	0.95	0.96

Table 5.4: The acceptance of the T2 minimum bias trigger (Acc.) and the contribution from low mass diffraction (Low M_X) to the acceptance of the different MCs.

due to different distributions of particles in pseudorapidity. Hence the classification result was corrected for the different probabilities. Since single diffractive events have over all lower multiplicities compared to double and non-diffractive and sometimes have no tracks in the T2 acceptance, the size of the correction was largest for them, with $\sim 17\,\%$ of events missed by T2 for SDL and SDR, whereas only $\sim 6\,\%$ of double diffractive and practically no non-diffractive events were missed. This correction was calculated from the training samples generated with P8-4C. This correction is dominated by the amount of low mass diffraction (here defined as events with all particles below T2 acceptance, $|\eta| > 6.5$). Hence, the maximum size of the correction and the systematic errors could be estimated from the difference of the inelastic cross-section obtained from the elastic one via the optical theorem and the directly measured inelastic cross-section with particles at $|\eta| \leq 6.5$, a measurement that was done at the collision energy of $\sqrt{s} = 7\,\text{TeV}$ and presented in Section 4.1. The results obtained there were $\sigma_{\text{inel},|\eta|>6.5} = (2.62 \pm 2.17)\,\text{mb}$ ($\sigma_{\text{inel},|\eta|>6.5} \leq 6.31\,\text{mb}$ at 95 % confidence). All the Monte Carlo samples studied gave acceptance corrections within these bounds. A comparison of the acceptance corrections obtained for the samples and the corrections calculated assuming only low mass events are missed can be seen in Table 5.4.

The raw fractions were corrected with the class-dependent T2 acceptance corrections in order to obtain the true fractions without event selection bias. Cross-sections obtained using these fractions and the inelastic cross-section as normalization, are shown in Table 5.5. The systematic uncertainties in the cross-sections comprised the full uncertainty of the inelastic cross-section measurement (normalization uncertainty), the method and bias (50 % of the bias) uncertainties and the trigger efficiency correction uncertainty (100 % of the correction). These uncertainties were summed in quadrature to obtain the full uncertainty. The cross-sections obtained were $\sigma_{\text{ND}} = 50.0 \pm 2.2\,\text{mb}$, $\sigma_{\text{DD}} = 8.7 \pm 0.9\,\text{mb}$ and $\sigma_{\text{SD}} = 16.0 \pm 3.5\,\text{mb}$ (the sum of the two SD configurations).

Some cross-checks of the diffractive cross-sections obtained with this method were done by limiting the definitions of the single- and double diffractive events to specific mass regions, where the previous CMS measurement[78] of diffractive cross-sections at $\sqrt{s} = 7\,\text{TeV}$ and preliminary TOTEM measurements[79, 80] of SD at $\sqrt{s} = 7\,\text{TeV}$ and $\sqrt{s} = 8\,\text{TeV}$ were done and events outside those mass regions

	Cross section [mb]						
	Val	**S+N**	**Syst**	**Bias**	**Acc**	**Sum**	**Exp**
				P8-4C			
ND	54.42	1.25	1.12		0.01	1.68	54.53
SDL	6.39	0.16	0.71		1.08	1.30	6.41
SDR	6.43	0.16	0.96		1.09	1.46	6.35
DD	7.45	0.18	0.29		0.44	0.56	7.40
Inel	74.70	1.70			2.60		74.70
				QGSJET			
ND	56.42	1.29	1.82	0.58	0.01	2.30	53.23
SDL	6.35	0.15	0.98	0.35	1.07	1.50	7.94
SDR	6.23	0.14	1.08	0.46	1.05	1.58	7.92
DD	5.70	0.13	0.11	0.11	0.34	0.40	5.61
Inel	74.70	1.70			2.46		74.70
				P8-MBR			
ND	53.33	1.23	0.38	0.55	0.01	1.40	53.58
SDL	6.59	0.17	0.68	0.37	1.11	1.36	6.14
SDR	6.50	0.16	0.51	0.48	1.10	1.32	6.21
DD	8.29	0.20	0.65	0.16	0.49	0.86	8.77
Inel	74.70	1.70			2.69		74.70
				P8-Monash			
ND	54.19	1.25	0.13	0.56	0.01	1.38	54.46
SDL	6.45	0.16	0.12	0.36	1.09	1.17	6.31
SDR	6.44	0.16	0.10	0.48	1.09	1.21	6.31
DD	7.61	0.19	0.06	0.15	0.45	0.51	7.62
Inel	74.70	1.70			2.62		74.70
				Data			
ND	50.03	1.14	1.82	0.33	0.01	2.17	
SDL	7.95	0.18	0.98	0.21	1.34	1.68	
SDR	8.07	0.19	1.08	0.29	1.36	1.77	
DD	8.65	0.20	0.65	0.10	0.51	0.86	
Inel	74.70	1.70			3.21		

Table 5.5: Obtained cross-sections (Val) and their uncertainties: statistical and normalization (S+N), systematic excluding bias correction (Syst), systematic from bias correction (Bias), acceptance correction (Acc) and the quadratic sum of all uncertainties (Sum) as well as the cross-sections expected based on generator-level information (Exp) for simulations and data.

were defined as non-diffractive. The results agreed within one standard deviation.

To make sure that the cross-sections obtained were not biased by any particular classification variables, the classification was repeated excluding different sets of variables: it was done excluding multiplicities, proton momentum losses or rapidity gap based variables. Results obtained with all the different sets of variables were compatible with the result obtained in the main analysis and with each other. It was also observed that single diffractive classification suffers when proton momentum losses are excluded. Rapidity gap and multiplicity based variables are not enough to assure symmetry between the left and right configurations.

Chapter 6

Conclusions and outlook

The cross-section measurements performed at the three energies (2.76, 7 and 8 TeV) and presented in this thesis gave results that were in good agreement with expectations. The values obtained were compatible with those obtained by other experiments. In Fig. 6.1 there is a comparison of the TOTEM 7 TeV results with those of the other LHC experiments. The measurements were also used to validate models of low-mass diffraction.

Results from some of the previous elastic, inelastic and total cross-section measurements and the inelastic ones that were presented in this thesis are shown in Fig. 6.2. The rise of the cross-section as a function of energy is observed both in the total and inelastic cross-section measurements. A reasonable agreement between model and experiment and between different measurements at the same energy is seen in all the points.

The classification of inelastic events allowed to determine the relative fractions of single, double and non-diffractive events that make up the inelastic cross-section using an innovative method. This information is important for further developments of models for non-perturbative QCD. The probabilities of observing diffractive events are related to the structure of the proton and understanding them helps to describe extensive air showers and to interpret high energy cosmic rays [85].

The process-specific cross-sections obtained were $\sigma_{\mathrm{ND}} = 50.0 \pm 2.2\,\mathrm{mb}$, $\sigma_{\mathrm{DD}} = 8.7 \pm 0.9\,\mathrm{mb}$ and $\sigma_{\mathrm{SD}} = 16.0 \pm 3.5\,\mathrm{mb}$. The non-diffractive cross-section obtained was quite low and on the other hand the single diffractive was quite high compared to prior expectations, but the results show reasonable agreement with most prior measurements of single and double diffractive cross-sections, of which several are shown in Figs. 6.3 and 6.4. Results shown with full lines follow the process definitions used in this thesis; diffractive events are those with rapidity gaps of three or more units in pseudorapidity. The results shown with dotted lines follow model-based definitions and are therefore not directly comparable.

Further total, elastic, inelastic and process-specific cross-section measurements at higher energies will help even further to understand the behaviour of the cross-sections as a function of energy and the dynamics behind the interactions.

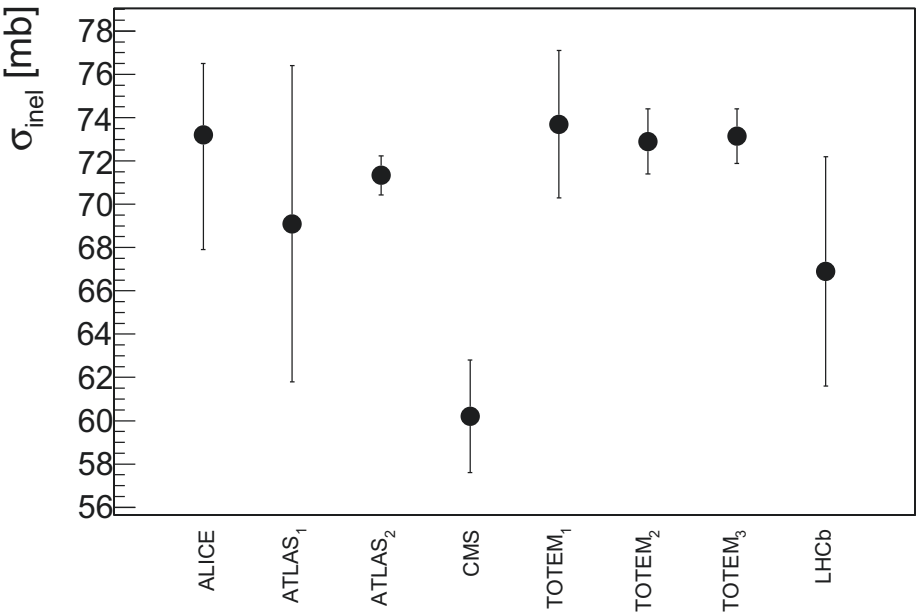

Figure 6.1: Comparison of inelastic (σ_{inel}) cross-section measurements by the different LHC experiments at $\sqrt{s} = 7$ TeV: ALICE[63], ATLAS[64, 81] (labelled ATLAS$_1$ and ATLAS$_2$), CMS[65], TOTEM[66, 67, 68] (TOTEM$_1$ is using the method based on CMS-luminosity, TOTEM$_2$ luminosity independent, TOTEM$_3$ based on elastic measurement) and LHCb[82]. Note that the CMS-result is limited to a kinematic range of $\xi > 5{*}10^{-6}$. ATLAS$_2$ and TOTEM$_3$ are based on an indirect measurement of the inelastic cross-section using the elastic and total cross-sections determined from elastic scattering using the Optical Theorem.

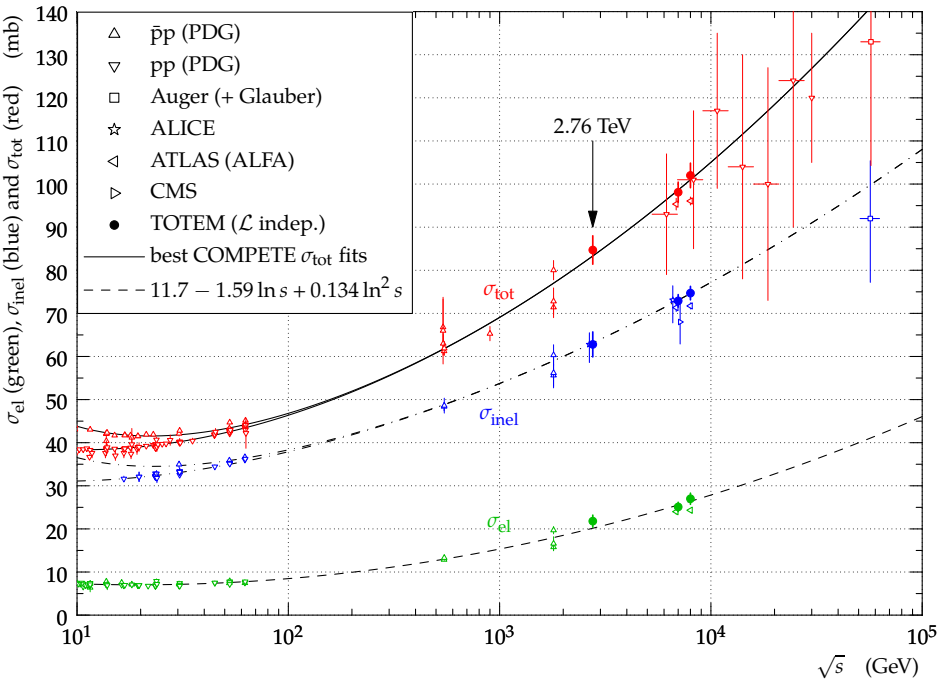

Figure 6.2: Total (σ_{tot}), inelastic (σ_{inel}) and elastic (σ_{el}) cross-section measurements at different energies and the best fits of the cross-section data by the COMPETE collaboration (lines).[13, 63, 64, 65, 68, 69, 83, 84]

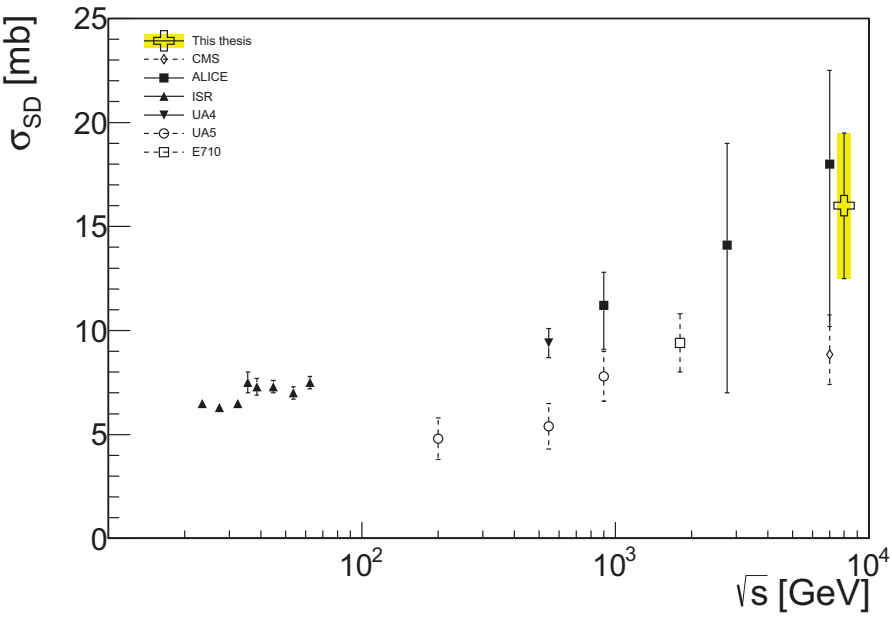

Figure 6.3: Single diffractive cross-sections as a function of $\sqrt{s}$ as measured by ALICE[18], ISR[86], UA5[87, 88], UA4[89], E710[90], CMS[78] and in this thesis.

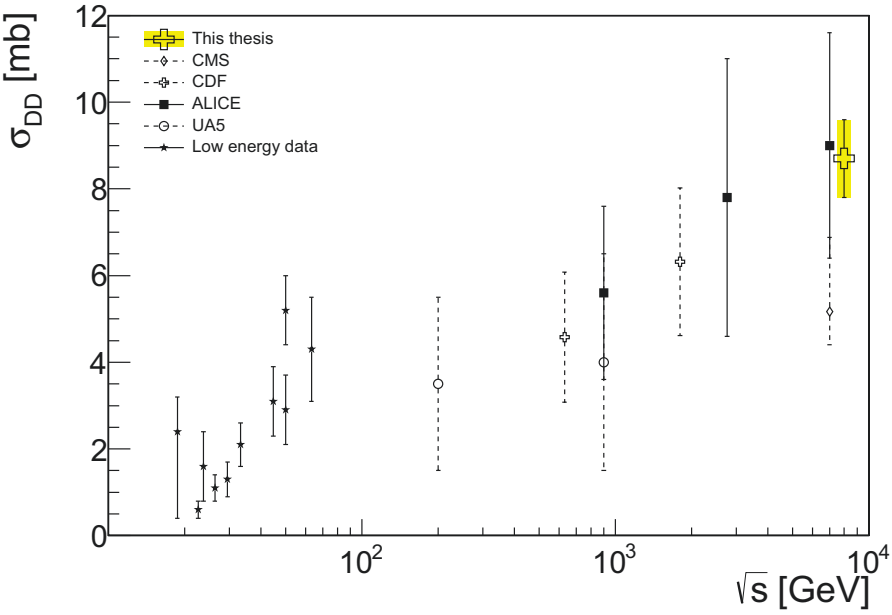

Figure 6.4: Double diffractive cross-sections as a function of $\sqrt{s}$ as measured by ALICE[18], UA5[88], CDF[91], CMS[78] and in this thesis. Various low energy data were taken from[92].

Detector acceptance in the forward region can be further extended by using for instance the CMS Forward Shower Counters (FSCs) [93], which would allow to improve the classification of inelastic events further. The FSCs detect particles in the pseudorapidity range $6 \leq |\eta| \leq 8$, which allows to improve separation between a certain type of double diffractive events, where one of the diffractive systems is entirely below the T2 acceptance ($|\eta| \geq 6.5$), and single diffractive events. Based on the information from the CMS central detectors and T2 these events have identical signatures if the proton of the single diffractive event is not seen in RPs. In double diffractive events, however, several particles are produced in the more forward pseudorapidities of which the FSCs cover some, whereas in the single diffractive events the FSC should be empty. This would allow to further reduce the uncertainties of the classification analysis, further improving the understanding of the proton structure.

Bibliography

[1] U. Amaldi *et al.*, Phys. Lett. B **44**, 112 (1973).

[2] U. Amaldi *et al.*, Nucl. Phys. B **145**, 367 (1978).

[3] L. Baksay *et al.*, Nucl. Phys. B **141**, 1 (1978).

[4] R. Battiston *et al.*, Phys. Lett. B **117**, 126 (1982).

[5] N. A. Amos *et al.*, Phys. Lett. B **243**, 158 (1990).

[6] F. Abe *et al.*, Phys. Rev. D **50**, 5550 (1994).

[7] S. Mandelstam, Phys. Rev. **112**, 1344 (1958).

[8] M. Froissart, Phys. Rev. **123**, 1053 (1961).

[9] A. Martin, Phys. Rev. D **80**, 065013 (2009).

[10] S. Ostapchenko, Nucl. Phys. B (Proc.Suppl.) **151**, 143 (2006).

[11] F. Halzen and A. Martin, *Quarks & Leptons: An Introductory Course in Modern Particle Physics* (John Wiley & Sons, 1984).

[12] G. Källén, *Elementary Particle Physics* (Addison-Wesley Publishing Company, Inc., 1964).

[13] COMPETE Collaboration, J. R. Cudell *et al.*, Phys. Rev. Lett. **89**, 201801 (2002).

[14] TOTEM Collaboration, G. Antchev *et al.*, Eur. Phys. J. C **76**, 661 (2016).

[15] TOTEM Collaboration, G. Anelli *et al.*, JINST **3**, S08007 (2008).

[16] V. Barone and E. Predazzi, *High-Energy Particle Diffraction* (Springer-Verlag, 2002).

[17] O. Nachtmann, Pomeron Physics and QCD, arXiv:hep-ph/0312279.

[18] ALICE Collaboration, B. Abelev *et al.*, Eur. Phys. J. C **73**, 2456 (2013).

[19] H1, C. Adloff *et al.*, Z. Phys. **C74**, 221 (1997).

[20] H1, S. Aid *et al.*, Z. Phys. **C70**, 609 (1996).

[21] H1, F. D. Aaron *et al.*, Eur. Phys. J. **C72**, 2074 (2012).

[22] ZEUS, H1, F. D. Aaron *et al.*, Eur. Phys. J. **C72**, 2175 (2012).

[23] R. A. Fisher, Annuals of Eugenics **7**, 179 (1936).

[24] B. P. Roe *et al.*, Nucl. Instr. Meth. Phys. Res. A **543**, 577 (2005).

[25] M. W. Gardner and S. R. Dorling, Atmos. Environ. **32**, 2627 (1998).

[26] J. Fürnkranz, J. Mach. Learn. Res. **2**, 721 (2002).

[27] T. Bayes, Philos. Trans. R. Soc. **53**, 370 (1763).

[28] A. Hoecker *et al.*, TMVA 4 Toolkit for Multivariate Data Analysis with ROOT users guide, CERN-OPEN-2007-007.

[29] CMS Collaboration, S. Chatrchyan *et al.*, JINST **3**, S08004 (2008).

[30] ATLAS Collaboration, G. Aad *et al.*, JINST **3**, S08003 (2008).

[31] LHCb Collaboration, A. Augosto Alves Jr. *et al.*, JINST **3**, S08005 (2008).

[32] ALICE collaboration, B. Abelev *et al.*, JINST **3**, S08002 (2008).

[33] L. Evans and P. Bryant, JINST **3**, S08001 (2008).

[34] M. Kramer and F. Soler, editors, *Large Hadron Collider Phenomenology* (Institute of Physics Publishing, 2004).

[35] TE-EPC-LPC in LHC, 2017, `http://te-epc-lpc.web.cern.ch/te-epc-lpc/machines/lhc/general.stm`.

[36] The Large Hadron Collider - CERN timelines, 2017, `https://timeline.web.cern.ch/timelines/The-Large-Hadron-Collider`.

[37] P. Aspell *et al.*, VFAT2: a front-end system on chip providing fast trigger information, digitized data storage and formatting for the charge sensitive readout of multi-channel silicon and gas particle detectors, in *Proceedings of TWEPP-07, Topical Workshop on Electronics for Particle Physics*, Prague, Czech Republic, 2007, `http://cdsweb.cern.ch/record/1069906`.

[38] M. Berretti, Development of reconstruction algorithms for inelastic processes studies in the totem experiment at lhc, Master's thesis, Siena U., 2008, `https://cds.cern.ch/record/1472954`.

[39] T. Sjöstrand *et al.*, JHEP **05**, 026 (2006).

[40] G. A. Schuler and T. Sjöstrand, Phys. Rev. D **49**, 2257 (1994).

[41] T. Sjöstrand *et al.*, Comput. Phys. Commun. **178**, 852 (2008).

[42] R. Engel, Z. Phys. C **66**, 203 (1995).

[43] R. Engel and J. Ranft, Phys. Rev. D **54**, 4244 (1996).

[44] A. Donnachie and P. V. Landshoff, Phys. Lett. B **296** (1992), hep-ph/9209205.

[45] B. Andersson, Camb. Monogr. Part. Phys. Nucl. Phys. Cosmol. **7**, 1 (1997).

[46] S. Navin, arXiv:1005.3894 [hep-ph].

[47] G. Ingelman and P. Schlein, Phys. Lett. B **152**, 256 (1985).

[48] R. Ciesielski and K. Goulianos, PoS ICHEP2012 , 301 (2013), arXiv:1205.1446 [hep-ph].

[49] R.Corke and T.Sjöstrand, JHEP **1103**, 032 (2011).

[50] P. Skands *et al.*, Eur. Phys. J. C **74**, 3024 (2014).

[51] A. Cappella *et al.*, Phys. Rep. **236**, 225 (1994).

[52] A. B. Kaidalov, Surveys in High Energy Physics **13**, 265 (1999), http://dx.doi.org/10.1080/01422419908244082.

[53] R. Engel, *PHOJET manual* (University of Siegen preprint, 1995).

[54] G. 't Hooft, Nuclear Physics B **72**, 461 (1974).

[55] R. Engel and J. Ranft, Hard diffraction and central diffraction in hadron-hadron and photon-hadron collisions, arXiv:hep-ph/9711383.

[56] V. Gribov, Sov. Phys. JETP **26**, 414 (1968).

[57] V. Gribov, Sov. Phys. JETP **29**, 483 (1969).

[58] S. Ostapchenko, Phys. Rev. D **74**, 014026 (2006).

[59] S. Ostapchenko, Phys. Rev. D **83**, 014018 (2011).

[60] S. Ostapchenko *et al.*, J. Phys. G: Nucl. Part. Phys. **28**, 2597 (2002).

[61] M. Baker and K. Ter-Martirosyan, Phys. Rep. **28**, 1 (1976).

[62] S. Ostapchenko, EPJ Web of Conferences **52**, 02001 (2013).

[63] ALICE Collaboration, B. Abelev *et al.*, Eur. Phys. J. C **73.6**, 1 (2013).

[64] ATLAS Collaboration, G. Aad *et al.*, Nat. Commun. **2**, 463 (2011).

[65] CMS Collaboration, S. Chatrchyan *et al.*, Phys. Lett. B **722**, 5 (2013).

[66] TOTEM Collaboration, G. Antchev *et al.*, Europhys. Lett. **101**, 21003 (2013).

[67] TOTEM Collaboration, G. Antchev *et al.*, Europhys. Lett. **101**, 21002 (2013).

[68] TOTEM Collaboration, G. Antchev *et al.*, Europhys. Lett. **101**, 21004 (2013).

[69] TOTEM Collaboration, G. Antchev *et al.*, Phys. Rev. Lett. **111**, 012001 (2013).

[70] K. Österberg, New results on elastic, diffractive and exclusive processes, DIS 2017, `https://indico.cern.ch/event/568360/contributions/2390670/attachments/1438189/2213522/KO_elastic_diffrative_lowx_DIS_april17_new.pdf`.

[71] M. Kuusela *et al.*, Int. J. Mod. Phys. A **25**, 1615 (2010).

[72] M. Kuusela *et al.*, AIP Conf. Proc. **1350**, 111 (2011).

[73] M. Mieskolainen, Bayesian Classification of Hadronic Diffraction in the Collider Detector at Fermilab, Master's thesis, Tampere University of Technology, 2013, `https://dspace.cc.tut.fi/dpub/handle/123456789/21965`.

[74] Minimum-bias and underlying event WG, 2017, `https://lpcc.web.cern.ch/lpcc/index.php?page=mb_ue_wg`.

[75] A. Hoecker *et al.*, PoS ACAT , 040 (2007), physics/0703039.

[76] CMS Collaboration, (2009), CMS PAS PFT-09-001.

[77] CMS Collaboration, (2010), CMS Note CMS-CR-2010-276.

[78] CMS Collaboration, V. Khachatryan *et al.*, Phys. Rev. D **92**, 012003 (2015).

[79] F. Oljemark and K. Österberg on behalf of the TOTEM collaboration, Studies of Soft Single Diffraction with TOTEM at the LHC at 7 TeV, Contribution to LHC students poster session 2013, `https://indico.cern.ch/event/238337/`.

[80] J. Mäntylä, Proton-Proton Single Diffractive Cross Section Measurement at $\sqrt{s} = 8$ TeV, special assignment, Engineering physics and mathematics, Aalto University, December 2015.

[81] ATLAS Collaboration, G. Aad *et al.*, Nucl. Phys. B **889**, 486 (2014).

[82] LHCb Collaboration, R. Aaij *et al.*, Measurement of the inelastic pp cross-section at a centre-of-mass energy of $\sqrt{s}$=7 tev, 2014, arXiv:1412.2500 [hep-ex].

[83] Particle Data Group, K. Nakamura *et al.*, J. Phys. G. Nucl. Part. Phys. **37**, 075021 (2010).

[84] Pierre Auger Collaboration, P. Abreu *et al.*, Phys. Rev. Lett. **109**, 062002 (2012).

[85] M. Ryskin *et al.*, Eur. Phys. J. C **54**, 199–217 (2008).

[86] J. Armitage *et al.*, Nucl. Phys. B **194**, 365 (1982).

[87] UA5 Collaboration, G. Alner *et al.*, Phys. Rep. **154**, 247 (1987).

[88] UA5 Collaboration, G. Alner *et al.*, Z. Phys. C **32**, 153 (1986).

[89] UA4 Collaboration, D. Bernard *et al.*, Phys. Lett. B **186**, 227 (1987).

[90] E710 Collaboration, N. Amos *et al.*, Phys. Lett. B **301**, 313 (1993).

[91] CDF Collaboration, T. Affolder *et al.*, Phys. Rev. Lett. **87**, 141802 (2001).

[92] C. Conta *et al.*, Nucl. Phys. B **175**, 97 (1980).

[93] M. Albrow *et al.*, Int. J. Mod. Phys. A **29**, 1446018 (2014).